



Spitzer/IRS Full Spectral Modeling to Characterize Mineralogical Properties of Silicate Dust in Heavily Obscured AGNs

T. Tsuchikawa¹ , H. Kaneda¹ , S. Oyabu² , T. Kokusho¹, H. Kobayashi¹, and Y. Toba^{3,4,5,6} ¹ Graduate School of Science, Nagoya University, Furo-cho, Chikusa-ku, Nagoya, Aichi 464-8602, Japan; kaneda@u.phys.nagoya-u.ac.jp² Institute of Liberal Arts and Sciences, Tokushima University, 1-1 Minami-Jyosanjiima, Tokushima-shi, Tokushima, 770-8502, Japan³ National Astronomical Observatory of Japan, 2-21-1 Osawa, Mitaka, Tokyo 181-8588, Japan⁴ Department of Astronomy, Kyoto University, Kitashirakawa-Oiwake-cho, Sakyo-ku, Kyoto 606-8502, Japan⁵ Academia Sinica Institute of Astronomy and Astrophysics, 11F of Astronomy-Mathematics Building, AS/NTU, No.1, Section 4, Roosevelt Road, Taipei 10617, Taiwan⁶ Research Center for Space and Cosmic Evolution, Ehime University, 2-5 Bunkyo-cho, Matsuyama, Ehime 790-8577, Japan

Received 2022 March 26; revised 2022 October 7; accepted 2022 October 15; published 2022 December 12

Abstract

Mid-infrared silicate dust bands observed in heavily obscured active galactic nuclei (AGNs) include information on the mineralogical properties of silicate dust. We aim to investigate the mineralogical picture of the circumnuclear region of heavily obscured AGNs to reveal obscured AGN activities through the picture. In our previous study, we investigated the properties of silicate dust in heavily obscured AGNs, focusing on the mineralogical composition and the crystallinity with Spitzer/IRS 5.3–12 μm spectra. In this study, we model the full-range Spitzer/IRS 5–30 μm spectra of 98 heavily obscured AGNs using a one-dimensional radiative transfer calculation with four dust species in order to evaluate wider ranges of the properties of silicate dust more reliably. Comparing fitting results between four dust models with different sizes and porosities, 95 out of the 98 galaxies prefer a porous silicate dust model without micron-sized large grains. The pyroxene mass fraction and the crystallinity are overall consistent with—but significantly different from—the previous results for the individual galaxies. The pyroxene-poor composition, small dust size, and high porosity are similar to newly formed dust around mass-loss stars as seen in our Galaxy, which presumably originates from the recent circumnuclear starburst activity. The high crystallinity on average suggests dust processing induced by AGN activities.

Unified Astronomy Thesaurus concepts: [Astrophysical dust processes \(99\)](#); [Infrared galaxies \(790\)](#); [Active galactic nuclei \(16\)](#)

Supporting material: figure set

1. Introduction

An active galactic nucleus (AGN) experiences actively evolving phases of supermassive black holes (SMBHs) by releasing the gravitational energy of accreting materials. The presence of AGN is classically diagnosed using optical high-excitation lines (e.g., Kauffmann et al. 2003b), which, however, reveals that the line diagnostics miss a significant fraction of AGNs, due to extinction by large amounts of dust surrounding AGNs. For example, more than 50% of optically non-Seyfert ultraluminous infrared galaxies (ULIRGs), whose infrared (IR) luminosities are defined to be higher than $10^{12} L_{\odot}$, were reported to host heavily obscured AGNs on the basis of IR spectral analyses (Imanishi et al. 2010; Ichikawa et al. 2014). The morphological structures of U/LIRGs tend to show signatures of galaxy interaction (Sanders & Mirabel 1996). Hydrodynamical simulations of the galaxy merger successfully reproduce various observed estimates such as the quasar luminosity function at each redshift (e.g., Hopkins et al. 2006). In these simulations, heavily obscured AGNs are predicted to be in an obscured phase of the nuclear growth before outflows blow out obscuring clouds, quench the star-forming activities and then evolve to unobscured AGNs. Indeed, recent observations revealed the ubiquitous presence of outflows

and/or inflows at the nuclear region in ULIRGs (e.g., Toba et al. 2017; Veilleux et al. 2020), suggesting dynamic evolutionary pictures of AGNs coupling with the surrounding material.

Silicate dust, which is a major component composing the cosmic dust, shows prominent spectral bands in the mid-IR wavelength range. The spectral features due to silicate dust have been detected in various kinds of astronomical objects, such as AGNs (e.g., Hao et al. 2007) as well as circumstellar disks or comets (e.g., Molster & Waters 2003; Henning 2010), through mid-IR spectroscopic observations with infrared space telescopes of ISO (Kessler et al. 1996), Spitzer (Werner et al. 2004), and AKARI (Murakami et al. 2007). Many papers have focused on the spectral profiles of the silicate dust bands of circumstellar and cometary dust in detail, and they have discussed evolutionary scenarios of the system or astrophysical phenomena. In contrast, few studies have systematically discussed the mid-IR spectra of heavily obscured AGNs for silicate dust properties in detail, although dust in heavily obscured AGNs is expected to be processed under more energetic and more dynamic environments than those surrounding the circumstellar or cometary dust.

Spoon et al. (2006) found crystallinity higher than 10% for several ULIRGs. They concluded that the high crystallinity originates from starburst activities, because the mid-IR crystalline features are detected only in absorption and thus the crystalline silicate is likely to be located far from the hot nucleus. On the other hand, Kemper et al. (2011) suggested that



Original content from this work may be used under the terms of the [Creative Commons Attribution 4.0 licence](#). Any further distribution of this work must maintain attribution to the author(s) and the title of the work, journal citation and DOI.

the starburst activities alone cannot explain such a high crystallinity; they concluded that additional crystallization mechanisms are needed other than the mass ejection from mass-loss stars in the starburst activities. Tsuchikawa et al. (2021) recently investigated the properties of silicate dust in heavily obscured AGNs using Spitzer/IRS archival data. They revealed that the crystallinity and the mineralogical olivine-to-pyroxene ratio are higher on average than those observed in the line of sight toward the diffuse interstellar medium (ISM) in our Galaxy. The olivine-rich mineralogical composition suggests that amorphous silicate, which presumably originates from starburst activities, is likely to be newly formed. Moreover, on the basis of the above studies, Tsuchikawa et al. (2021) consider a scenario of dust processing in which amorphous silicate newly formed by starburst activities is crystallized in regions close to the nucleus by the AGN activities and is then transported to cooler regions by outflows.

It is important to investigate other properties of amorphous silicate dust, such as grain size and porosity, to discuss the dust processing scenario in more detail. As an example of silicate dust processing observed in our Galaxy, it is reported that amorphous silicate dust around YSOs is larger in size than that in the diffuse ISM, indicating dust growth therein (e.g., Juhász et al. 2010). Tsuchikawa et al. (2021) conducted spectral fitting to the $10\ \mu\text{m}$ absorption feature of the silicate dust bands, which did not constrain the size or porosity of amorphous silicate; the bottom profile of the $10\ \mu\text{m}$ absorption feature is easily blurred by increases in the polycyclic aromatic hydrocarbon (PAH) or unobscured hot dust emission. Thus, spectral fitting for the full wavelength range of $5\text{--}30\ \mu\text{m}$ is important. A caveat of the full-range spectral fitting is the radiative transfer effect. Indeed, apparent optical depth ratios of the $10\text{--}18\ \mu\text{m}$ amorphous silicate features of heavily obscured AGNs cannot be reproduced by the model in Tsuchikawa et al. (2021) assuming a simple full-screen obscuration. Sirocky et al. (2008) reproduced the optical depth ratios of heavily obscured AGNs by performing a radiative transfer calculation, and constrained geometrical properties of the dust distribution or dust opacity models though the dust distribution in Sirocky et al. (2008) cannot approximate a clumpy AGN torus as done, e.g., by Siebenmorgen et al. (2015). Hence, in the present study, we apply a model analysis to the full-range IRS spectra of heavily obscured AGNs, including the wavelength range longer than $12\ \mu\text{m}$, which was outside the fitting range in the previous study, using a radiative transfer calculation to determine wider ranges of properties of silicate dust more reliably. On the basis of the dust properties thus obtained, we discuss the origin of each dust species or dust processing scenarios to imply a physical picture of the circumnuclear region of heavily obscured AGNs. Throughout the paper, we calculate the luminosity distance to the galaxies assuming the cosmological parameters $H_0 = 70\ \text{km s}^{-1}\ \text{Mpc}^{-1}$, $\Omega_\Lambda = 0.7$, and $\Omega_m = 0.3$.

2. The Sample

We selected the mid-IR spectra of nearby heavily obscured AGNs from the sample of Tsuchikawa et al. (2021), which were observed by the low-resolution mode of the InfraRed Spectrograph (IRS; Houck et al. 2004) on board the Spitzer Space Telescope. The sample of the previous study was selected by the following three criteria: (1) the apparent optical depth of the $10\ \mu\text{m}$ silicate feature larger than 1.5, (2) the

equivalent width of the $6.2\ \mu\text{m}$ PAH emission smaller than $270\ \text{nm}$, and (3) the redshift lower than 0.35. The mid-IR spectra of the sample were retrieved from the Cornell AtlaS of Spitzer/IRS Sources (CASSIS; Lebouteiller et al. 2011) version LR7 as done in Tsuchikawa et al. (2021). In this study, we analyzed the spectra in the full IRS spectral range. Because of the robustness of the analysis, we added a selection criterion that the apparent optical depth at $17\ \mu\text{m}$ is larger than 0.2. We adopted a power-law function used in Imanishi (2009) for the absorption-free continuum, which was determined with the anchor points at 14.2 and $24\ \mu\text{m}$. By the additional criterion for the present study, 98 out of the 115 objects in the previous sample, the general properties of which are summarized in Table 1, were selected. We performed the spectral stitching as described in the previous study as well. We did not use the bonus segments of the LL order ($19.4\text{--}21.7\ \mu\text{m}$), because of mismatch between the first and second orders.

3. Modeling of the Full-range IRS Spectra

For the purpose of modeling the full-range IRS spectra, it is important to determine the mid-IR continuum shape. The continuum emission is likely to originate from the dust heated by AGN. Tsuchikawa et al. (2021) applied a power-law plus spline function simply assuming a full-screen obscuration by silicate dust to reproduce the AGN-heated dust continuum emission. Although the model used in Tsuchikawa et al. (2021) is a good approximation for the narrow wavelength range of $5.3\text{--}12\ \mu\text{m}$, it cannot well reproduce the full-range $5\text{--}30\ \mu\text{m}$ spectra in our sample. The full-screen dust obscuration model overpredicts the apparent optical depth of the $18\ \mu\text{m}$ silicate feature compared to the $10\ \mu\text{m}$ silicate feature. As described in Section 1, this is likely due to a radiative transfer effect, as the effective absorption becomes shallower at longer wavelengths, assuming that the continuum source at longer wavelengths is located farther from the nucleus (e.g., Imanishi et al. 2006; Spoon et al. 2006; Sirocky et al. 2008). The spectral modelings of the full-range IRS spectra of heavily obscured AGNs were performed by several papers. Marshall et al. (2007) and Stierwalt et al. (2013, 2014) reproduced the IRS spectra using multicomponent dust emission models with extinction curves of our Galaxy. On the other hand, Siebenmorgen & Krügel (2007), for instance, modeled the spectra by a radiative transfer calculation, considering realistic geometry of the dust distribution. However, these studies did not focus on the optical properties of silicate dust in detail, and thus could not obtain good fits for the silicate features as a whole. In this study, we achieve very good fits to the full-range IRS spectra in our sample, as shown in Figure 1, by modeling dust properties in detail and numerically calculating the radiative transfer of dusty shells. The radiative transfer modeling of the AGN-heated dust emission, F_d^{agn} , is explained in the following subsections.

We cannot reproduce the sample spectra by the component of F_d^{agn} alone; a significant fraction of the sample spectra clearly show the $6\text{--}8\ \mu\text{m}$ absorption features due to H_2O ice and hydrogenated amorphous carbon (HAC). We reproduced these features using the three templates derived in Tsuchikawa et al. (2021) and Gaussian functions by multiplying the extinction term of $\exp(-\tau_{\text{ice}})$ to F_d^{agn} , the parameters of which were fixed at the same values as those in Tsuchikawa et al. (2021). Furthermore, we newly added two broad absorption components at ~ 4.7 and $12\ \mu\text{m}$, which are most probably due to CO gas rovibrational and H_2O ice libration modes,

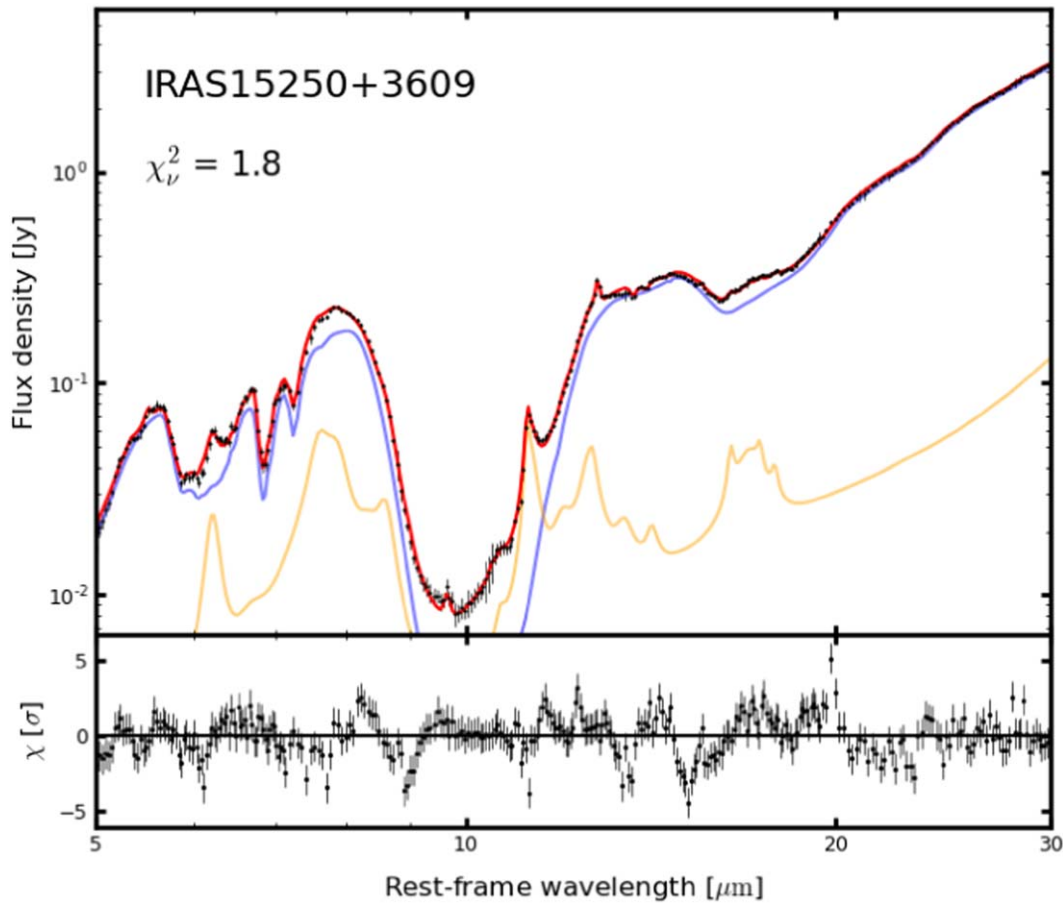


Figure 1. An example result of the mid-IR 5–30 μm spectral modeling of heavily obscured AGNs. The black points and the red solid line show the observed spectrum and the best-fit model of IRAS 15250+3609. The blue solid line represents the AGN-heated dust emission components with ice absorption, $F_d^{\text{agn}} \exp(-\tau_{\text{ice}})$, while the yellow lines represent the SF-heated dust and PAH emission, F_{sf} , and the line emission components. We show the reduced χ^2 value in the upper left corner. The residual spectrum normalized by the errors is depicted in the bottom panel.

respectively. For the opacity profiles of the 4.7 and 12 μm absorptions, we used a Gaussian function and an absorption coefficient of a 0.1 μm sized homogeneous sphere of 10 K pure H_2O ice, respectively. The central wavelength and full width at half maximum of the Gaussian function for the 4.7 μm feature were fixed at 4.8 μm and 0.75 μm , respectively. The absorption coefficient for the 12 μm feature was calculated via the Mie theory using the optical constants measured by Hudgins et al. (1993). We also took into account unobscured hot dust emission heated by AGN in order to model the flat profile at the bottom of the 10 μm silicate absorption feature as mentioned in Tsuchikawa et al. (2021). We adopted the average spectrum of quasars obtained by Hao et al. (2007) for the spectral profile of the AGN-heated unobscured hot dust component.

It is necessary to consider an emission component due to the PAH and dust heated by SF activity, F_{sf} , as well. In general, the inter-band ratios of the PAH emission vary among galaxies. For example, the strength ratio of the C–C stretching at 5–9 μm to C–H bending at 9–15 μm features is known to depend on the ionization degree of the PAH molecules (Draine & Li 2007). The average size of the PAHs also affects the inter-band ratios. Maaskant et al. (2014) show that AGN spectra tend to have relatively high ratios of the 17 μm complex in comparison to the other shorter-wavelength features, which indicates that large PAHs are abundant in AGNs. Moreover, for partially extended sources, the ratio of the PAH emission to the AGN-

heated dust emission is expected to be higher in LL spectra than in SL spectra, because the slit size of the LL module is larger than that of the SL module.

Marshall et al. (2007) modeled the dust and PAH emission spectra typical of starburst galaxies with the templates derived from the spectra of NGC 7714 and the average spectra of the starburst galaxies in Brandl et al. (2006), respectively. They determined the relative strengths of the individual PAH emission bands using PAHFIT (Smith et al. 2007), which can decompose the PAH emission component of a mid-IR spectrum with a multicomponent Drude function. In this study, we adopted the models by Marshall et al. (2007) for the SF-heated dust and PAH emission models. In order to perform spectral fitting with a moderate degree of freedom, we decomposed the PAH model by Marshall et al. (2007) into the four components of F_{pah6} , F_{pah7} , F_{pah11} , and F_{pah17} according to the central wavelengths of the PAH bands described by the Drude profiles as follows:

$$F_{\text{sf}} = C_{\text{sf}} (f_{\text{dust}/7} F_{\text{d}}^{\text{sf}} + f_{6/7} F_{\text{pah6}} + F_{\text{pah7}} + f_{11/7} F_{\text{pah11}} + f_{17/7} F_{\text{pah17}}) \frac{1 - \exp(-\tau_{\text{sf}})}{\tau_{\text{sf}}}, \quad (1)$$

where C_{sf} is the amplitude of F_{sf} , and $f_{\text{dust}/7}$, $f_{6/7}$, $f_{11/7}$, and $f_{17/7}$ are the amplitude ratios of the individual components to F_{pah7} . The individual four PAH components of F_{pah6} , F_{pah7} ,

Table 1
General Properties of the Sample

Name (1)	AORkey (2)	R.A. (J2000) (3)	Decl. (J2000) (4)	z (5)	$\log L_{\text{IR}} (L_{\odot})$ (6)
IRAS 00091–0738	10440960, 10108928	00 ^h 11 ^m 43 ^s .2	−07 ^d 22 ^m 06 ^s	0.1184	12.27 ± 0.07
IRAS F00183–7111	7556352	00 ^h 20 ^m 34 ^s .6	−70 ^d 55 ^m 26 ^s	0.3270	12.95 ± 0.09
IRAS 00188–0856	4962560	00 ^h 21 ^m 26 ^s .4	−08 ^d 39 ^m 27 ^s	0.1284	12.41 ± 0.09
IRAS 00397–1312	4963584	00 ^h 42 ^m 15 ^s .4	−12 ^d 56 ^m 03 ^s	0.2617	12.94 ± 0.19
IRAS 00406–3127	4964096	00 ^h 43 ^m 03 ^s .1	−31 ^d 10 ^m 49 ^s	0.3424	12.80 ± 0.15
IRAS 01166–0844SE	10441984, 10109952	01 ^h 19 ^m 07 ^s .8	−08 ^d 29 ^m 12 ^s	0.1180	12.12 ± 0.13
IRAS 01199–2307	4964864	01 ^h 22 ^m 20 ^s .8	−22 ^d 51 ^m 57 ^s	0.1562	12.31 ± 0.13
IRAS 01298–0744	4965120	01 ^h 32 ^m 21 ^s .4	−07 ^d 29 ^m 08 ^s	0.1362	12.36 ± 0.12
IRAS 01355–1814	4965376	01 ^h 37 ^m 57 ^s .4	−17 ^d 59 ^m 20 ^s	0.1920	12.48 ± 0.11
IRAS F01478+1254	23012864	01 ^h 50 ^m 28 ^s .4	+13 ^d 08 ^m 58 ^s	0.1470	11.98 ± 0.39
IRAS 01569–2939	10110208	01 ^h 59 ^m 13 ^s .7	−29 ^d 24 ^m 34 ^s	0.1400	12.26 ± 0.11
IRAS 02455–2220	4967680	02 ^h 47 ^m 51 ^s .2	−22 ^d 07 ^m 38 ^s	0.2840	12.70 ± 0.15
IRAS 02530+0211	6652160	02 ^h 55 ^m 34 ^s .4	+02 ^d 23 ^m 41 ^s	0.0276	11.05 ± 0.05
IRAS 03158+4227	12256256	03 ^h 19 ^m 11 ^s .9	+42 ^d 38 ^m 25 ^s	0.1344	12.61 ± 0.08
NGC 1377 ^a	9511424	03 ^h 36 ^m 40 ^s .1	−20 ^d 54 ^m 02 ^s	0.0060	10.17 ± 0.03
IRAS 03538–6432	4968192	03 ^h 54 ^m 25 ^s .2	−64 ^d 23 ^m 44 ^s	0.3007	12.79 ± 0.10
IRAS 03582+6012	20341504	04 ^h 02 ^m 32 ^s .9	+60 ^d 20 ^m 41 ^s	0.0300	11.40 ± 0.09
IRAS 04074–2801	25185536	04 ^h 09 ^m 30 ^s .4	−27 ^d 53 ^m 43 ^s	0.1537	12.25 ± 0.11
IRAS 04313–1649	4968960	04 ^h 33 ^m 37 ^s .0	−16 ^d 43 ^m 31 ^s	0.2680	12.67 ± 0.11
IRAS 04384–4848	6650880	04 ^h 39 ^m 50 ^s .8	−48 ^d 43 ^m 17 ^s	0.2035	12.40 ± 0.07
ESO 203–IG001	20334080	04 ^h 46 ^m 49 ^s .5	−48 ^d 33 ^m 30 ^s	0.0529	11.85 ± 0.04
IRAS 05020–2941	25185792	05 ^h 04 ^m 00 ^s .7	−29 ^d 36 ^m 54 ^s	0.1544	12.38 ± 0.06
IRAS F06076–2139	20359680	06 ^h 09 ^m 45 ^s .7	−21 ^d 40 ^m 24 ^s	0.0374	11.63 ± 0.04
IRAS 06206–6315	4969984	06 ^h 21 ^m 00 ^s .8	−63 ^d 17 ^m 23 ^s	0.0924	12.22 ± 0.04
IRAS 06301–7934	4970240	06 ^h 26 ^m 42 ^s .2	−79 ^d 36 ^m 30 ^s	0.1564	12.39 ± 0.06
IRAS 06361–6217	4970496	06 ^h 36 ^m 35 ^s .7	−62 ^d 20 ^m 31 ^s	0.1596	12.41 ± 0.10
IRAS 07251–0248	20346112	07 ^h 27 ^m 37 ^s .6	−02 ^d 54 ^m 54 ^s	0.0876	12.41 ± 0.08
IRAS 08201+2801	18202112	08 ^h 23 ^m 12 ^s .6	+27 ^d 51 ^m 40 ^s	0.1678	12.30 ± 0.14
IRAS F08520–6850	20343808	08 ^h 52 ^m 32 ^s .0	−69 ^d 01 ^m 54 ^s	0.0451	11.74 ± 0.04
IRAS 08572+3915	4972032	09 ^h 00 ^m 25 ^s .3	+39 ^d 03 ^m 54 ^s	0.0584	12.15 ± 0.03
IRAS 09539+0857	10444032, 11676160	09 ^h 56 ^m 34 ^s .3	+08 ^d 43 ^m 05 ^s	0.1289	12.10 ± 0.19
IRAS F10038–3338	20352256	10 ^h 06 ^m 04 ^s .6	−33 ^d 53 ^m 06 ^s	0.0342	11.71 ± 0.05
IRAS 10091+4704	4973824	10 ^h 12 ^m 16 ^s .7	+46 ^d 49 ^m 42 ^s	0.2460	12.65 ± 0.10
IRAS 10173+0828	14838528, 20314880	10 ^h 20 ^m 00 ^s .2	+08 ^d 13 ^m 34 ^s	0.0491	11.80 ± 0.12
IRAS F10237+4720	22117632	10 ^h 26 ^m 48 ^s .2	+47 ^d 05 ^m 07 ^s	0.0589	11.48 ± 0.11
IRAS 10378+1109	4974336	10 ^h 40 ^m 29 ^s .1	+10 ^d 53 ^m 17 ^s	0.1363	12.35 ± 0.09
IRAS 10485–1447	10444800, 10105088	10 ^h 51 ^m 03 ^s .0	−15 ^d 03 ^m 22 ^s	0.1330	12.22 ± 0.16
IRAS 11028+3130	18203392	11 ^h 05 ^m 37 ^s .5	+31 ^d 14 ^m 31 ^s	0.1986	12.42 ± 0.14
IRAS 11038+3217	4975104	11 ^h 06 ^m 35 ^s .7	+32 ^d 01 ^m 46 ^s	0.1300	11.62 ± 0.35
IRAS 11095–0238	4975360	11 ^h 12 ^m 03 ^s .3	−02 ^d 54 ^m 24 ^s	0.1066	12.28 ± 0.08
IRAS 11130–2659	10105600	11 ^h 15 ^m 31 ^s .5	−27 ^d 16 ^m 22 ^s	0.1361	12.14 ± 0.15
IRAS 11180+1623	18203648	11 ^h 20 ^m 41 ^s .7	+16 ^d 06 ^m 56 ^s	0.1660	12.31 ± 0.14
IRAS 11223–1244	4976128	11 ^h 24 ^m 50 ^s .7	−13 ^d 01 ^m 16 ^s	0.1990	12.57 ± 0.10
IRAS 11506+1331	10445312, 10111488	11 ^h 53 ^m 14 ^s .1	+13 ^d 14 ^m 26 ^s	0.1273	12.35 ± 0.10
IRAS 11524+1058	18203904	11 ^h 55 ^m 05 ^s .1	+10 ^d 41 ^m 22 ^s	0.1787	12.23 ± 0.15
IRAS 11582+3020	4976384	12 ^h 00 ^m 46 ^s .8	+30 ^d 04 ^m 14 ^s	0.2230	12.57 ± 0.17
IRAS 12032+1707	4976896	12 ^h 05 ^m 47 ^s .7	+16 ^d 51 ^m 08 ^s	0.2178	12.63 ± 0.17
IRAS 12127–1412	10445824, 10105856	12 ^h 15 ^m 19 ^s .1	−14 ^d 29 ^m 41 ^s	0.1330	12.20 ± 0.13
IRAS F12224–0624	20367104	12 ^h 25 ^m 03 ^s .9	−06 ^d 40 ^m 52 ^s	0.0264	11.24 ± 0.08
NGC 4418	4935168	12 ^h 26 ^m 54 ^s .6	−00 ^d 52 ^m 40 ^s	0.0073	11.04 ± 0.05
IRAS 12359–0725	10106112	12 ^h 38 ^m 31 ^s .6	−07 ^d 42 ^m 25 ^s	0.1380	12.18 ± 0.22
IRAS 12447+3721	25187840	12 ^h 47 ^m 07 ^s .7	+37 ^d 05 ^m 36 ^s	0.1580	12.17 ± 0.20
IRAS F13045+2354	4168448	13 ^h 07 ^m 00 ^s .6	+23 ^d 38 ^m 04 ^s	0.2750	12.61 ± 0.23
IRAS 13106–0922	25186048	13 ^h 13 ^m 14 ^s .6	−09 ^d 38 ^m 08 ^s	0.1745	12.57 ± 0.22
IRAS F13279+3401	12235264	13 ^h 30 ^m 15 ^s .2	+33 ^d 46 ^m 29 ^s	0.0230	10.46 ± 0.15
IRAS 13352+6402	4979968	13 ^h 36 ^m 51 ^s .1	+63 ^d 47 ^m 04 ^s	0.2366	12.55 ± 0.10
Mrk 273	4980224	13 ^h 44 ^m 42 ^s .1	+55 ^d 53 ^m 13 ^s	0.0378	12.15 ± 0.03
IRAS 14070+0525	4980992	14 ^h 09 ^m 31 ^s .2	+05 ^d 11 ^m 31 ^s	0.2644	12.82 ± 0.12
IRAS F14394+5332	29040128	14 ^h 41 ^m 04 ^s .3	+53 ^d 20 ^m 08 ^s	0.1045	12.10 ± 0.06
IRAS F14511+1406	4168960	14 ^h 53 ^m 31 ^s .5	+13 ^d 53 ^m 58 ^s	0.1390	11.93 ± 0.20
IRAS F14554+3858	28244224	14 ^h 57 ^m 22 ^s .7	+38 ^d 46 ^m 28 ^s	0.0735	11.10 ± 0.29
IRAS 15225+2350	10112512	15 ^h 24 ^m 43 ^s .9	+23 ^d 40 ^m 10 ^s	0.1390	12.17 ± 0.09
IRAS 15250+3609	4983040	15 ^h 26 ^m 59 ^s .3	+35 ^d 58 ^m 37 ^s	0.0552	12.05 ± 0.05

Table 1
(Continued)

Name (1)	AORkey (2)	R.A. (J2000) (3)	Decl. (J2000) (4)	z (5)	$\log L_{\text{IR}} (L_{\odot})$ (6)
Arp 220	4983808	15 ^h 34 ^m 57 ^s .2	+23 ^d 30 ^m 11 ^s	0.0181	12.17 ± 0.03
FESS J160655.82+541500.7	24189952	16 ^h 06 ^m 55 ^s .8	+54 ^d 15 ^m 00 ^s	0.2060	... ^c
IRAS F16073+0209	17546496	16 ^h 09 ^m 49 ^s .7	+02 ^d 01 ^m 30 ^s	0.2230	12.35 ± 0.27
IRAS 16090–0139	4984576	16 ^h 11 ^m 40 ^s .4	−01 ^d 47 ^m 05 ^s	0.1336	12.57 ± 0.04
IRAS F16156+0146	17546752	16 ^h 18 ^m 09 ^s .3	+01 ^d 39 ^m 22 ^s	0.1320	12.11 ± 0.13
IRAS F16242+2218	17547008	16 ^h 26 ^m 26 ^s .0	+22 ^d 11 ^m 45 ^s	0.1570	11.74 ± 0.29
IRAS F16305+4823	22135040	16 ^h 31 ^m 58 ^s .7	+48 ^d 17 ^m 22 ^s	0.0874	11.92 ± 0.08
IRAS 16300+1558	4985088	16 ^h 32 ^m 21 ^s .4	+15 ^d 51 ^m 45 ^s	0.2417	12.74 ± 0.11
IRAS 16455+4553	14875136	16 ^h 46 ^m 58 ^s .9	+45 ^d 48 ^m 22 ^s	0.1906	12.37 ± 0.09
IRAS 16468+5200W	10107136	16 ^h 48 ^m 01 ^s .3	+51 ^d 55 ^m 43 ^s	0.1500	12.11 ± 0.11
IRAS 16468+5200E	10106880	16 ^h 48 ^m 01 ^s .6	+51 ^d 55 ^m 44 ^s	0.1500	12.11 ± 0.11
IRAS 17044+6720	10107904	17 ^h 04 ^m 28 ^s .4	+67 ^d 16 ^m 28 ^s	0.1349	12.17 ± 0.08
IRAS F17028+3616	27194112	17 ^h 04 ^m 33 ^s .5	+36 ^d 12 ^m 18 ^s	0.0851	11.15 ± 0.43
IRAS 17068+4027	4986112	17 ^h 08 ^m 32 ^s .1	+40 ^d 23 ^m 28 ^s	0.1790	12.40 ± 0.10
IRAS 17208–0014	4986624	17 ^h 23 ^m 21 ^s .9	−00 ^d 17 ^m 00 ^s	0.0428	12.40 ± 0.04
IRAS 17463+5806	4987392	17 ^h 47 ^m 04 ^s .7	+58 ^d 05 ^m 22 ^s	0.3090	12.64 ± 0.11
IRAS 17540+2935	18204928	17 ^h 55 ^m 56 ^s .1	+29 ^d 35 ^m 26 ^s	0.1081	11.87 ± 0.09
IRAS 18443+7433	4987904	18 ^h 42 ^m 54 ^s .7	+74 ^d 36 ^m 21 ^s	0.1347	12.32 ± 0.08
IRAS 18531–4616	4988160	18 ^h 56 ^m 53 ^s .0	−46 ^d 12 ^m 46 ^s	0.1408	12.33 ± 0.22
IRAS 18588+3517	18205440	19 ^h 00 ^m 41 ^s .1	+35 ^d 21 ^m 27 ^s	0.1067	11.97 ± 0.10
IRAS 20100–4156	4989696	20 ^h 13 ^m 29 ^s .8	−41 ^d 47 ^m 34 ^s	0.1296	12.64 ± 0.06
IRAS 20109–3003	14875904	20 ^h 14 ^m 05 ^s .5	−29 ^d 53 ^m 53 ^s	0.1407	11.98 ± 0.26
IRAS 20286+1846	18205696	20 ^h 30 ^m 54 ^s .4	+18 ^d 56 ^m 37 ^s	0.1358	12.20 ± 0.26
IRAS 20551–4250	4990208	20 ^h 58 ^m 26 ^s .7	−42 ^d 39 ^m 01 ^s	0.0430	12.06 ± 0.03
IRAS 21077+3358	18205952	21 ^h 09 ^m 50 ^s .6	+34 ^d 10 ^m 34 ^s	0.1767	12.41 ± 0.45
IRAS 21272+2514	4990464	21 ^h 29 ^m 29 ^s .3	+25 ^d 27 ^m 55 ^s	0.1508	12.30 ± 0.39
IRAS F21329–2346	10448640, 10108160	21 ^h 35 ^m 45 ^s .8	−23 ^d 32 ^m 34 ^s	0.1251	12.15 ± 0.10
IRAS 22088–1831W	25189120	22 ^h 11 ^m 33 ^s .7	−18 ^d 17 ^m 06 ^s	0.1702	12.44 ± 0.12
IRAS 22088–1831E	25189376	22 ^h 11 ^m 33 ^s .8	−18 ^d 17 ^m 05 ^s	0.1702	12.44 ± 0.12
IRAS 22116+0437	18206464	22 ^h 14 ^m 10 ^s .3	+04 ^d 52 ^m 26 ^s	0.1938	12.33 ± 0.27
NGC 7479 ^b	22093312	23 ^h 04 ^m 56 ^s .6	+12 ^d 19 ^m 22 ^s	0.0079	10.76 ± 0.06
IRAS 23129+2548	4991488	23 ^h 15 ^m 21 ^s .4	+26 ^d 04 ^m 32 ^s	0.1789	12.48 ± 0.12
IRAS F23234+0946	10449152, 10108416	23 ^h 25 ^m 56 ^s .2	+10 ^d 02 ^m 50 ^s	0.1279	12.15 ± 0.11
IRAS 23230–6926	4992000	23 ^h 26 ^m 03 ^s .5	−69 ^d 10 ^m 20 ^s	0.1066	12.31 ± 0.04
IRAS 23365+3604	4992512	23 ^h 39 ^m 01 ^s .2	+36 ^d 21 ^m 09 ^s	0.0645	12.17 ± 0.06

Notes. Column 1: the name of the object. Column 2: AORkey (Spitzer/IRS identification number). Columns 3 and 4: the position of the object. Column 5: the redshift cited from the NASA/IPAC Extragalactic Database (NED). Column 6: the total 8–1000 μm IR luminosity, which is calculated from the IRAS fluxes with the definition by Sanders & Mirabel (1996).

^a The spectrum of NGC 1377 is unavailable in CASSIS. The spectral data were retrieved from the summary of the SINGS Legacy project (Kennicutt et al. 2003; SINGS Team 2020) in the NASA/IPAC IR Science Archive (IRSA).

^b The SL order 2 spectrum of NGC 7479 is unavailable in CASSIS. It was retrieved from the Spitzer Heritage Archive (SHA).

^c The IR fluxes cannot be obtained. Thus, its IR luminosity cannot be calculated.

F_{pah11} , and F_{pah17} consist of multicomponent Drude functions whose central wavelengths are in ranges of 5–7 μm , 7–9 μm , 11–15 μm , and longer than 15 μm , respectively. Within the individual four PAH components, the inter-band ratios of the Drude functions were fixed. $f_{\text{dust}/7}$, $f_{6/7}$, $f_{11/7}$ and $f_{17/7}$ were constrained within plausible ranges on the basis of the variations of the PAH features in the starburst galaxies studied by Smith et al. (2007) and Draine et al. (2021), which are summarized in Table 2. The term of $(1 - \exp(-\tau_{\text{sf}}))/\tau_{\text{sf}}$ reproduces the extinction for the SF-heated dust and PAH emission assuming a well-mixed geometry. The extinction curve observed in the line of sight toward the Galactic center (Chiar & Tielens 2006) was used for the wavelength dependence of the optical depth, τ_{sf} . Tsuchikawa et al. (2021) considered an additional feature at 10.68 μm , which is

likely due to dehydrogenated PAHs (Mackie et al. 2015). We incorporated it into the PAH model with the strength ratio of F_{pah11} to the 10.68 μm feature fixed at the value obtained from the average spectra of the starburst galaxies in Brandl et al. (2006). In addition, both of the AGN-originated and SF-originated atomic and molecular line emissions were reproduced by Gaussian functions in the same way as in Tsuchikawa et al. (2021).

3.1. Radiative Transfer Calculation

We calculated the AGN-heated dust emission, $F_{\text{d}}^{\text{agn}}$, using the one-dimensional dust radiative transfer code DUSTY (Ivezic & Elitzur 1997). DUSTY performs a self-consistent radiative transfer simulation, assuming a simple spatial distribution and the thermal equilibrium of dust. We assume

Table 2
Free Parameters for the Mid-IR Spectral Modeling

Parameter	Description	Range	Grid for Calculation with DUSTY AGN-heated Dust Emission
C_d^{agn}	Amplitude of F_d^{agn}	[0, ∞]	...
f_{BB}	Fractional contribution of the blackbody of 1000 K	[0, ∞]	...
$\tau_{\text{lib, peak}}$	Amplitude of the absorption due to the H ₂ O ice libration mode	[0, ∞]	...
$C_{\text{unobs}}^{\text{agn}}$	Amplitude of the unobscured AGN-heated dust emission	[0, ∞]	...
SF-heated dust and PAH emission			
C_{sf}	Amplitude of the SF-heated dust and PAH emission	[0, ∞]	...
$f_{\text{cont}/7}$	SF-heated dust to PAH 7.7 μm emission ratio	[0.3, 1.5]	...
$f_{6/7}$	PAH 6.2-to-7.7 μm emission ratio	[0.7, 1.5]	...
$f_{11/7}$	PAH 11.2-to-7.7 μm emission ratio	[0.5, 3]	...
$f_{17/7}$	PAH 17-to-7.7 μm emission ratio	[0.5, 2]	...
$\tau_{\text{sf, 9.7}}$	Peak dust extinction for the SF-heated dust and PAH emissions	[0.3, 1.5]	...
Dust composition ratios			
r_{py}	Mass ratio of amorphous pyroxene to total amorphous silicate	[0, 40]%	0, 10, 20, 30, 40
r_{cr}	Mass ratio of crystalline to total silicate	[0, 20]%	0, 5, 10, 15, 20
r_{si}	Mass ratio of silicate to total dust	[60, 97]%	60, 65, 70, 75, 80, 85, 90, 95, 97
Geometrical properties			
p	Power-law index of the radial density profile	[0.5, 2.0]	0.5, 1.0, 1.5, 2.0
Y	Ratio of the outer to inner radius of the dust shell	log [25, 800]	25, 50, 100, 200, 400, 800
τ_V	Dust optical depth at the wavelength of 550 nm	[10, 400]	10, 20, 30, 40, 50, 60, 70, 80, 90, 100, 110, 120, 130, 140, 150, 160, 170, 180, 190, 200, 210, 220, 230, 240, 260, 300, 350, 400

a spherically symmetric dust distribution. Such a simplified geometry cannot approximate a clumpy AGN torus (e.g., Siebenmorgen et al. 2015). A power-law function was adopted for the radial mass density profile using the power-law index p , as described by $\rho(r) = \rho_0 r^{-p}$. The radial mass density was normalized by the radial optical depth at the optical wavelength of 0.55 μm , $\tau_V = (\kappa_{\text{abs},V} + \kappa_{\text{sca},V}) \rho_0 \int_{r_{\text{in}}}^{r_{\text{out}}} r^{-p} dr$, where the mass absorption and scattering coefficients of dust, $\kappa_{\text{abs},\lambda}$ and $\kappa_{\text{sca},\lambda}$, are assumed to be spatially uniform. The wavelength dependences of $\kappa_{\text{abs},\lambda}$ and $\kappa_{\text{sca},\lambda}$, which include information on dust properties, are described in the next subsection. The inner radius of the spherically symmetric dust distribution, r_{in} , is determined by the dust sublimation. While the sublimation temperature of dust depends on dust species, DUSTY does not allow us to set different sublimation temperatures between the dust species. Therefore, we simply assumed 1000 K as the sublimation temperature of all the dust species. The outer radius, r_{out} , is defined using the ratio of the outer to inner radii of dust cloud, Y , as $Y = r_{\text{out}}/r_{\text{in}}$. We adopted the spectrum of an accretion disk empirically derived by Schartmann et al. (2005) for the heating source buried in the dust cloud. The source spectrum consists of a broken power-law function for the wavelength range of 0.01–10 μm and a 1000 K Planck function for wavelengths longer than 10 μm .

We tentatively fitted the sample spectra by the model described above to find that the above model often underestimates the 5–8 μm continuum of the sample spectra. For a significant fraction of our sample of AGNs, obscured outflows were detected (Veilleux et al. 2020). Hence, we need to consider the contribution from the shock heating or the obscured polar dust emission, and thus introduce another obscured hot dust component using a Planck function with a fixed temperature of 1000 K. The hot dust component is assumed to be obscured by the dust shell considered in the

DUSTY calculation, as described by

$$F_d^{\text{agn}} = C_d^{\text{agn}} (F_{\text{DUSTY}} + f_{\text{BB}} B_\nu(1000 \text{ K}) e^{-\tau_{\text{ext}}}), \quad (2)$$

where F_{DUSTY} and $B_\nu(1000 \text{ K})$ correspond to the output spectrum of the DUSTY calculation and the blackbody emission spectrum with 1000 K, respectively. Here, C_d^{agn} , f_{BB} , and τ_{ext} are the amplitude of F_d^{agn} , the fractional contribution of the blackbody component, and the radial optical depth due to dust extinction, respectively.

3.2. Dust Properties

We constructed dust opacity models with the optical properties of amorphous olivine, amorphous pyroxene, crystalline olivine, and amorphous carbon, which were obtained by the experimental measurements, as summarized in Table 3 and Figure 2. As shown in the upper panels of Figure 2, amorphous olivine and pyroxene have different peak wavelengths of ~ 9.7 and $\sim 9.3 \mu\text{m}$, respectively. Tsuchikawa et al. (2019) found difference in the wing of the 10 μm silicate feature of heavily obscured AGNs at shorter wavelengths. Thus, we incorporated amorphous olivine and pyroxene into the dust model for the purpose of reproducing the difference in the wing of the 10 μm feature. The upper panels of Figure 2 also show that the mid-IR 5–8 μm extinctions of amorphous olivine and pyroxene are quite small, compared to the 10 μm feature. Hence, if a radiative transfer calculation is performed, considering only silicate as the dust species, the wings of the silicate feature are likely to be seen in the emission while the peak lies in the absorption (Kemper et al. 2002). The typical extinction curves observed in our Galaxy (e.g., Lutz 1999; Indebetouw et al. 2005), however, show relatively large mid-IR extinction as compared to the silicate features. Therefore, amorphous carbon (ACH2; Colangeli et al. 1995) is newly introduced in this study. The mid-IR absorption coefficient of amorphous carbon

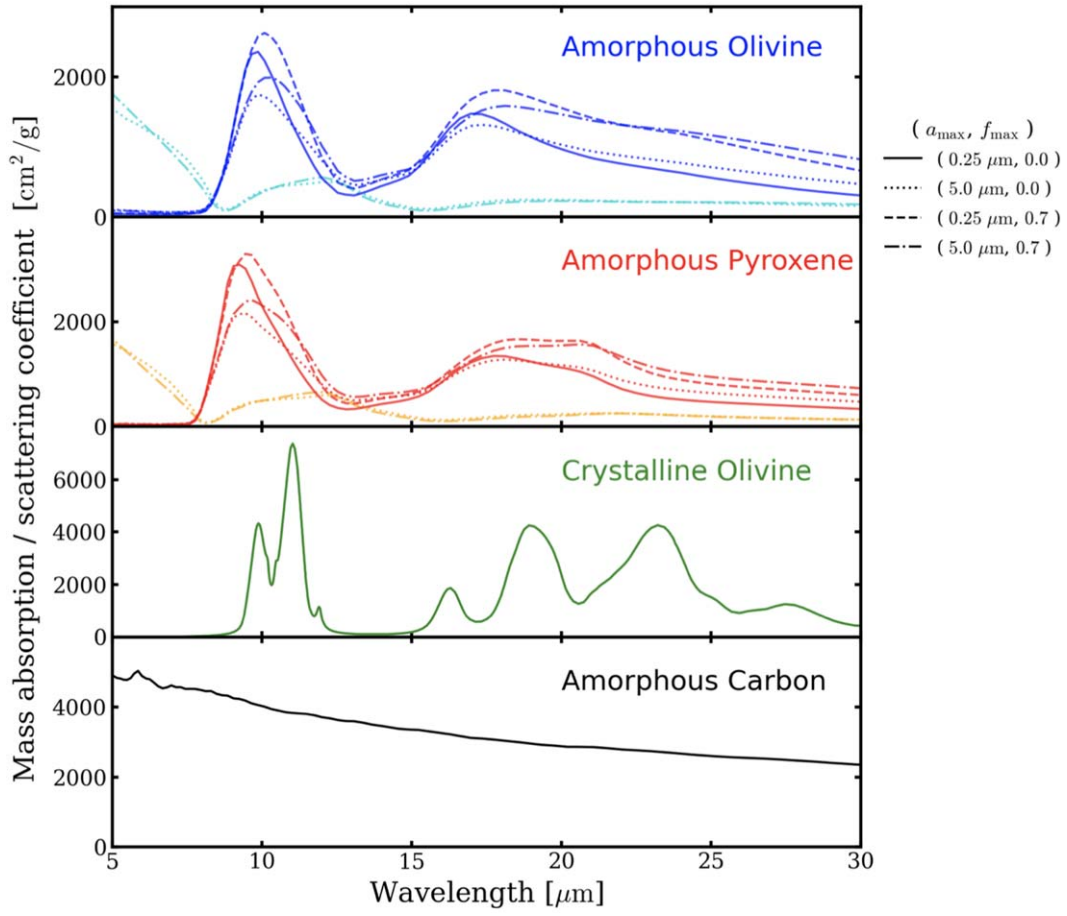


Figure 2. Mass absorption and scattering coefficients of amorphous olivine (top), amorphous pyroxene (upper middle), crystalline olivine (lower middle), and amorphous carbon (bottom). In the panels of amorphous olivine and pyroxene, the mass absorption and scattering coefficients calculated with different f_{\max} and a_{\max} are shown with different line styles. The cyan and orange lines show the mass scattering coefficients, and the other colors show the mass absorption coefficients. The mass scattering coefficients of amorphous olivine and pyroxene calculated with $a_{\max} = 0.25 \mu\text{m}$, crystalline olivine and amorphous carbon are much smaller than their mass absorption coefficients and therefore are not visible in the figure.

Table 3
Dust Properties Used in This Study

Dust Species	Chemical Formula	Mass Density (g/cc)	a_{\max}^a (μm)	f_{\max}^b	Wavelength Range (μm)	References ^c
Amorphous Olivine	MgFeSiO ₄	3.71	0.25/5.0	0.0/0.7	0.01–0.20	1
					0.20–500	2
Amorphous Pyroxene	Mg _{0.5} Fe _{0.5} SiO ₃	3.20			0.01–0.20	1
					0.20–500	2
Crystalline Olivine	Mg _{1.72} Fe _{0.21} SiO ₄	3.30	0.25	0.7	0.01–7.5	3
			Rayleigh	...	7.5–500	4
Amorphous Carbon	C	1.81	0.25	0.7	0.01–0.04	5
					0.04–500	6

Notes.

^a The maximum size of the MRN dust size distribution. The optical properties of crystalline olivine at the wavelengths longer than $7.5 \mu\text{m}$ are calculated with the Rayleigh limit.

^b The maximum vacuum fraction for DHS. The optical properties of crystalline olivine at the wavelengths longer than $7.5 \mu\text{m}$ are derived by a statistical method of DFF, not the DHS.

^c References for the optical constants: (1) Draine & Hensley 2021; (2) Dorschner et al. 1995; (3) Pitman et al. 2013; (4) Zeidler et al. 2015; (5) Hagemann et al. 1975; (6) Colangeli et al. 1995.

Table 4

Summary of the Four Dust Models Used in the Full-range Spectral Analysis

Model	Description	a_{\max} (μm)	f_{\max}
1	Homogeneous spherical/small-sized grain	0.25	0.0
2	Homogeneous spherical/large-sized grain	5.0	0.0
3	Porous/small-sized grain	0.25	0.7
4	Porous/large-sized grain	5.0	0.7

is relatively flat, as shown in Figure 2, and thus we can enhance the 5–8 μm extinction compared to the 10 μm silicate feature by increasing the relative abundance of amorphous carbon.

We calculated the mass absorption and scattering coefficients, κ_{abs} and κ_{sca} , of all the dust species except crystalline olivine, using the Distribution of Hollow Spheres (DHS; Min et al. 2003, 2005) for the classical MRN dust size distribution (Mathis et al. 1977). The MRN dust size distribution is described by a power-law function as

$$\frac{dn}{da} \propto a^{-3.5} \quad (a_{\min} \leq a \leq a_{\max}), \quad (3)$$

where a is the dust size. The minimum value of the dust size, a_{\min} , was fixed at 0.005 μm , while we tested two maximum values, a_{\max} , of 0.25 and 5.0 μm . The former dust size distribution satisfies the Rayleigh limit in the mid-IR range. Kemper et al. (2004) and Min et al. (2007) reproduced the silicate feature observed in the diffuse ISM in our Galaxy with the Rayleigh limit. DHS enables us to consider internal inhomogeneity by averaging the optical properties calculated for various volume fractions of the internal vacuum of the hollow sphere, f , for a uniform distribution within $0 \leq f \leq f_{\max}$. We applied 0 and 0.7 to f_{\max} , and thus tested the four models as summarized in Table 4. $f_{\max} = 0$ is equivalent to a homogeneous spherical dust model. For the purpose of calculating κ_{abs} and κ_{sca} of amorphous carbon, a_{\max} and f_{\max} were fixed at 0.25 μm and 0.7, respectively, which are expected for diffuse ISM silicate in our Galaxy, as the detailed properties of carbonaceous dust are out of scope in this study.

The opacity of crystalline silicate shows sharp spectral features in the mid-IR range, and hence its sensitivity to the grain morphology as well as the mineralogical composition is greater than that of amorphous silicate. For example, it is known that a simple Mie calculation with a homogeneous spherical grain does not reproduce the astronomical or experimental data of crystalline silicate at all (e.g., Fabian et al. 2001). The Distribution of Form Factor (DFF) model, which was developed by Min et al. (2006), is more flexible for the grain morphology than a similar statistical approach of the DHS. In the DFF model, the mass absorption coefficient is calculated assuming the Rayleigh limit, as follows:

$$\kappa_{\text{abs}} = \frac{2\pi}{\rho\lambda} \int_0^1 \text{Im} \frac{P(L)}{1/(\epsilon - 1) + L} dL, \quad (4)$$

where ρ , L , and $P(L)$ are the mass density, the form factor, and the form factor distribution, respectively. Zeidler et al. (2015) obtained $P(L)$ by fitting to the IR spectra of an olivine powder measured by Tamanai et al. (2006) with the optical constants of crystalline olivine (the San Carlos olivine; $\text{Mg}_{1.72}\text{Fe}_{0.21}\text{SiO}_4$) using the DFF model. In the present study, we obtained the

optical properties of the crystalline olivine with the DFF model assuming the optical constants measured at 300 K and $P(L)$ by Zeidler et al. (2015) for the three crystallographic axes, and averaged the optical properties over the axes. The κ_{abs} is shown in the lower middle panel of Figure 2. We also obtained κ_{abs} and κ_{sca} of crystalline olivine for the wavelength range shorter than 7.5 μm in the same way as for amorphous silicate with $a_{\max} = 0.25 \mu\text{m}$, $f_{\max} = 0.7$ and with the optical constants measured by Pitman et al. (2013). For the purpose of the radiative transfer calculation, we gridded the three dust mass ratios of amorphous pyroxene to total amorphous silicate, r_{pyr} , crystalline to total silicate, r_{cry} , and silicate to total dust, r_{si} . We calculated the dust continuum spectra, F_{DUSTY} , for 151,200 grid points for the geometrical and mineralogical parameter space of p , Y , τ_{V} , r_{pyr} , r_{cry} , and r_{si} as shown in Table 2.

3.3. Determination of the Model Parameters

We estimated the model parameters that best reproduce the sample spectra, using the four models summarized in Table 4, via the following steps: first, we conducted spectral fitting within narrow wavelength ranges to estimate the parameters of gas and ice absorption and PAH and line emission components. The maximum likelihood method with the Levenberg–Marquardt algorithm was used in the spectral fittings. In the subsequent steps, the amplitudes of the CO gas absorption and all the line emission components were fixed at the values obtained in the first step. Second, we performed the full-range spectral fitting of all the 151,200 grid points in the geometrical and mineralogical parameter space shown in Table 2, and searched for the best-fit grid point. The same fitting algorithm as in the previous step was used. The 10 parameters of the AGN-heated dust and the SF-heated dust and PAH emission components shown in Table 2 were set to be free. We adopted the ice and PAH parameters obtained in the previous step as the initial parameters.

In the second step, the sampling of the parameter grid for the sake of the radiative transfer calculation is too coarse to estimate the uncertainties of the parameters from the probability distribution weighted by $\exp(-\chi^2/2)$ on the basis of the Bayesian statistics (e.g., Kauffmann et al. 2003a). Thus, we performed a multidimensional log-linear interpolation of the parameter grid to approximate F_{DUSTY} in Equation (2) in a continuous parameter space, and determined the posterior probability distributions of all the parameters in Table 2 using a Markov Chain Monte Carlo (MCMC) method. Emcee v3, which is a Python package implementing the affine invariant ensemble sampler (Goodman & Weare 2010; Foreman-Mackey et al. 2013), was used for the MCMC code. We applied uniform prior distributions for the plausible parameter ranges shown in Table 2. The MCMC was started from a small ball around the best-fit parameters obtained in the second step. We set an ensemble of 64 “walkers,” which are the Markov chains evolving in parallel, and ran the MCMC algorithm with 11,000 steps, discarding the first 1000 steps as a “burn-in” period. We adopted the best-fit step out of the 10,000 steps for the resultant parameter set, which are used in the following sections. The 16th and 84th percentiles of the posterior distributions were adopted for the lower and upper uncertainties, respectively.

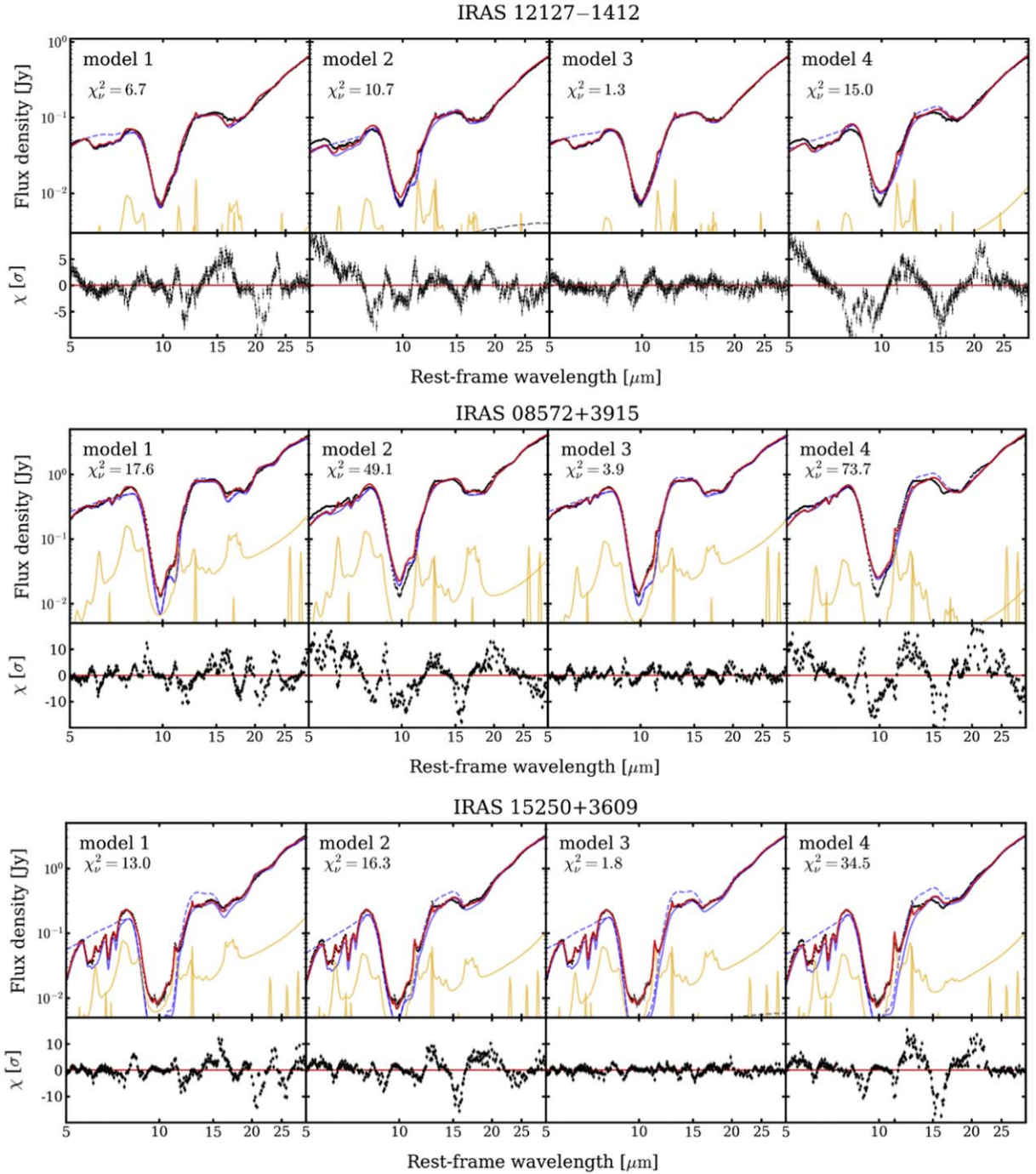


Figure 3. Examples of mid-IR spectral fits with models 1 (left), 2 (middle left), 3 (middle right), and 4 (right) to example spectra of IRAS 12127-1412, IRAS 08572+3915, and IRAS 15250+3609. The best-fit spectrum by each model is shown with the red solid line. The blue dashed and solid lines represent the AGN-heated dust emission components without ice absorption, F_d^{agn} , and with ice absorption, $F_d^{\text{agn}} \exp(-\tau_{\text{ice}})$, respectively, while the yellow lines represent the SF-heated dust and PAH emission, F_{sf} , and the line emission components. We show the reduced χ^2 values in the upper left corner in each panel.

4. Results

We fitted all the spectra in our sample within the 5–30 μm range with the four models, considering the dust radiative transfer effects. Figure 3 shows typical examples of the fitting results with the four dust models, indicating that all the four models do well at reproducing the overall profiles, such as the band ratio of the 10–18 μm features and the continuum shape,

while the detailed quality of the fits is different between the models. We find that model 1 with $f_{\text{max}} = 0.0$ does not reproduce the central wavelength of the 18 μm amorphous feature, while model 3 with $f_{\text{max}} = 0.7$ reproduces it well, owing to the peak shift of the 18 μm feature. This trend is commonly seen for most of our sample spectra. We compared the reduced χ^2 values between the models in Figure 4, which indicates that

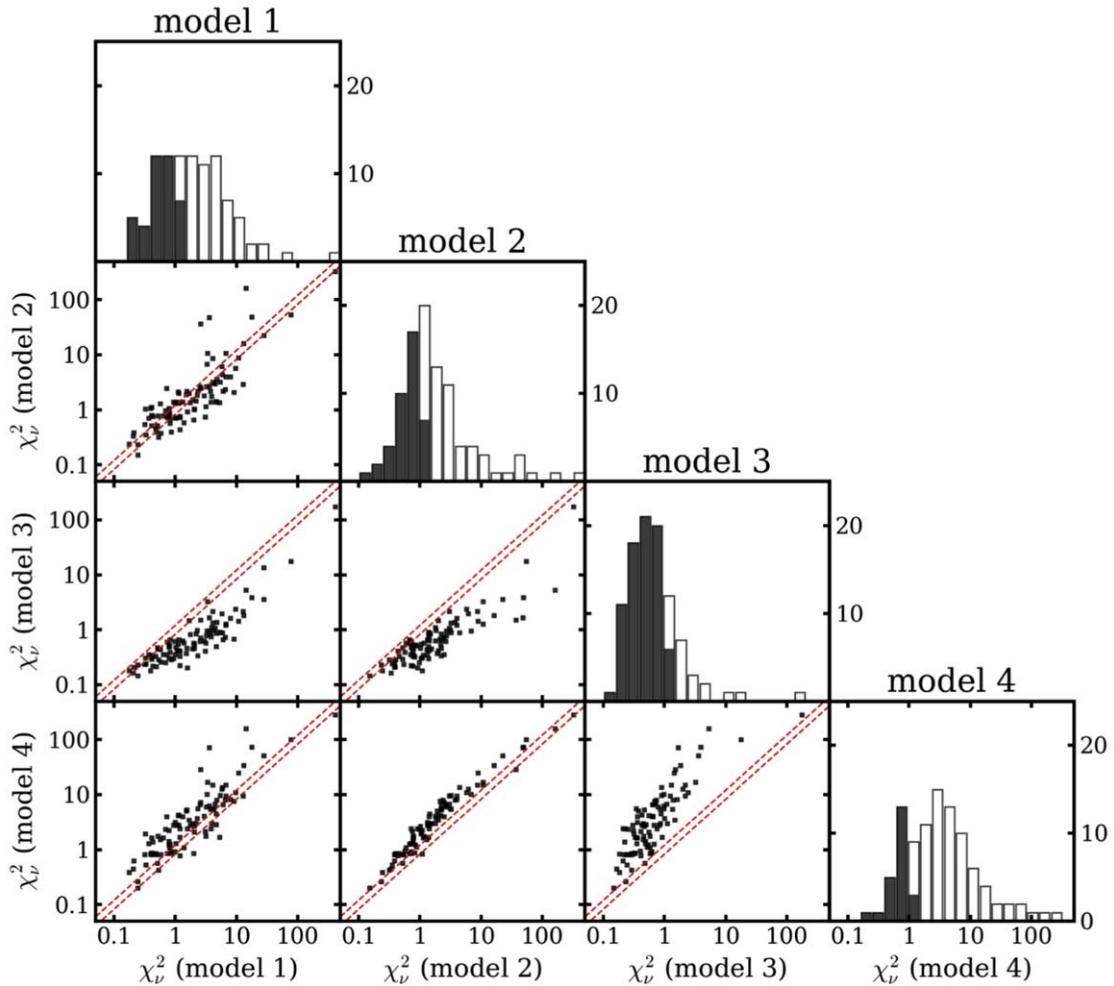


Figure 4. Comparison between the results of the four models. The panels at the diagonal positions show the histograms of reduced χ^2 of each model. Black and white bars represent the objects, the fits of which are accepted and rejected, respectively, with a significance level of 5%. The scatter plots at lower diagonal positions are the relationship between the reduced χ^2 values of different two models. Red dashed lines show the thresholds at which the χ^2 between two models are significantly different, with a significance level of 5% on the basis of F-test.

model 3 gives better fitting results than model 1 for 96 out of the 98 objects in our sample, and their differences are significant for 88 out of the 96 objects with a significance level of 5% by F-test.

Alternatively, model 2, in which we consider larger dust sizes, also shows the peak shift of the 10 and 18 μm features as compared to that of model 1 in Figure 2. However, the fits by model 2 do not improve as much as those by model 3. Comparing the reduced χ^2 values between all the spectra, 97 out of the 98 objects prefer model 3, the porous and small-sized dust model, to model 2, and their differences are significant for 88 out of the 97 objects. This is likely owing to high scattering efficiency of large-sized dust as shown in Figure 2 as well as a peak shift smaller than model 3. In the wavelength range where scattering is more effective, a photon travels a longer distance in the cloud on average before escaping the cloud, and thus the dust extinction is enhanced. Indeed, Figure 3 shows that the best-fit results of models 2 and 4, in which larger dust sizes are considered, deviate from the observed spectra at around 5 and 12 μm , where the scattering coefficients are relatively high.

We also confirm that model 4 cannot reproduce the sample spectra better than model 3. In conclusion, model 3, which assumes the small size and porous structure, best reproduces 95 out of the 98 spectra of heavily obscured AGNs in our sample.

Although models 1 and 2 are preferred by two and one out of the 98 objects, respectively, the preference is not statistically significant. Figure set 5 shows the modeling results of the full-range Spitzer/IRS spectra in our sample with model 3. We can recognize that model 3 reproduces our sample spectra considerably well. Hence, we use the results of model 3 for all the objects in the sample below.

In addition to the dust size and the porosity, we obtain the mineralogical composition of amorphous silicate and the crystallinity with model 3. The pyroxene mass fraction, r_{pyr} , and the crystallinity, r_{cry} , thus obtained are summarized in Appendix. Figure 6 shows the histograms of the dust properties of the r_{pyr} and r_{cry} in this study. The histogram of r_{pyr} shows a distribution skewed to the left, the 16th, 50th (median), and 84th percentiles of which are 0.5%, 5.1%, and 11.6%, respectively. The histogram of r_{cry} shows a relatively uniform distribution in a range of 0%–14%, the 16th, 50th (median) and 84th percentiles of which are 3.0%, 5.8%, and 8.2%, respectively. Tsuchikawa et al. (2021) also derived the abundances of the amorphous pyroxene and crystalline silicate, in which the radiative transfer effects were not considered, but a simple full-screen obscuration by dust was assumed despite the overprediction of the apparent optical depth of the 18 μm silicate feature compared to the 10 μm feature. In addition,

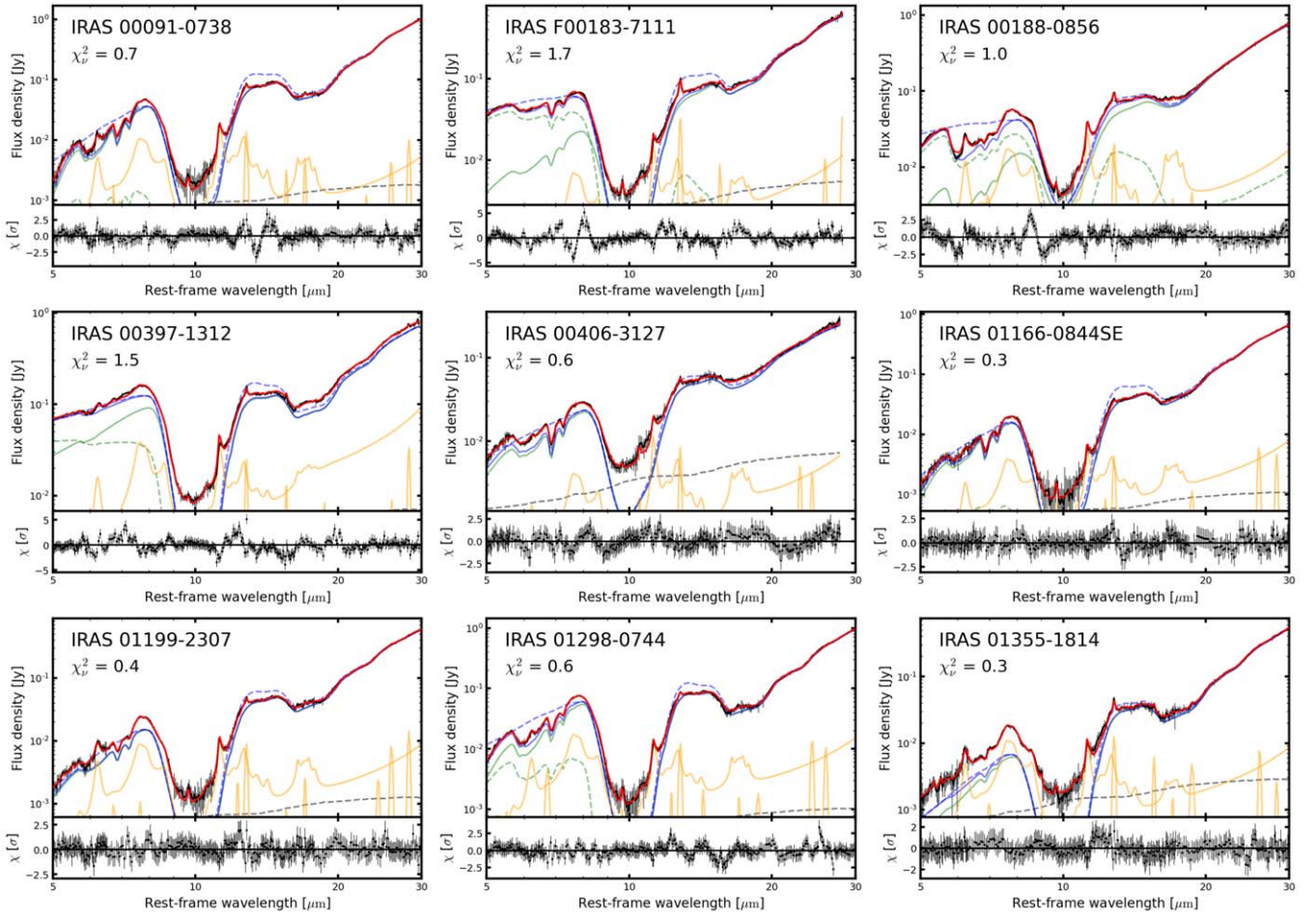


Figure 5. Examples of the modeling results of the mid-IR 5–30 μm spectra of heavily obscured AGNs. The best-fit spectrum is shown with the red solid line. The blue dashed and solid lines represent the AGN-heated dust emission components without ice absorption, F_d^{agn} , and with ice absorption, $F_d^{\text{agn}} \exp(-\tau_{\text{ice}})$, respectively, while the yellow lines represent the SF-heated dust and PAH emission, F_{sf} , and the line emission components. The AGN-heated dust emission component (blue solid line) is decomposed into two components: the dust emission calculated by DUSTY (green solid line) and the additional obscured hot dust emission (green dashed line). The gray dashed line shows the emission component due to the unobscured hot dust heated by AGN. We show the reduced χ^2 values in the upper left corner in each panel. The complete figure set (98 images) is available in the online journal.

(The complete figure set (98 images) is available.)

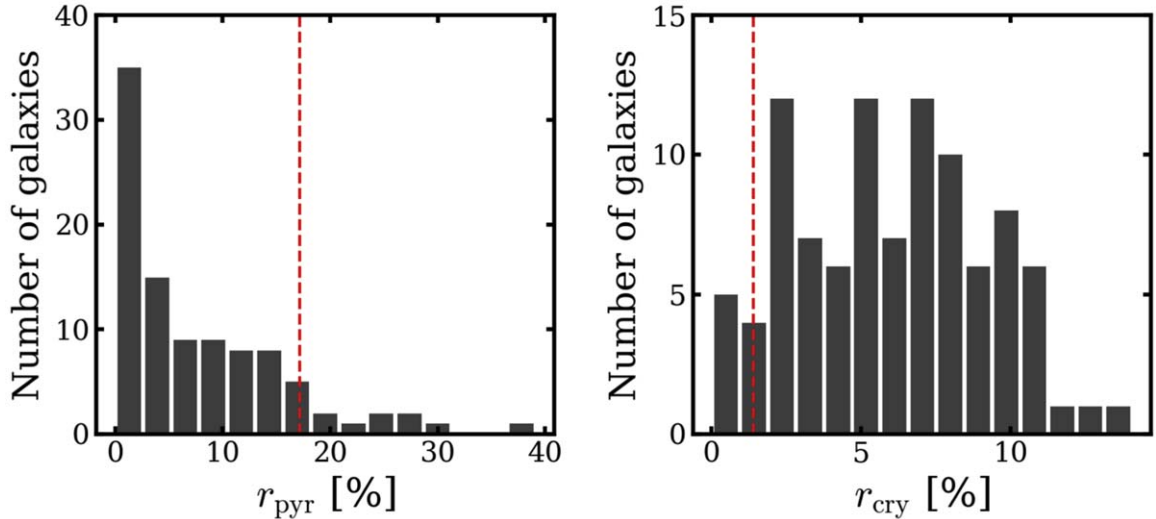


Figure 6. Histograms of the pyroxene mass fraction, r_{pyr} , and the crystallinity, r_{cry} . Red dashed lines correspond to typical dust properties of the diffuse ISM observed in our Galaxy (Do-Duy et al. 2020).

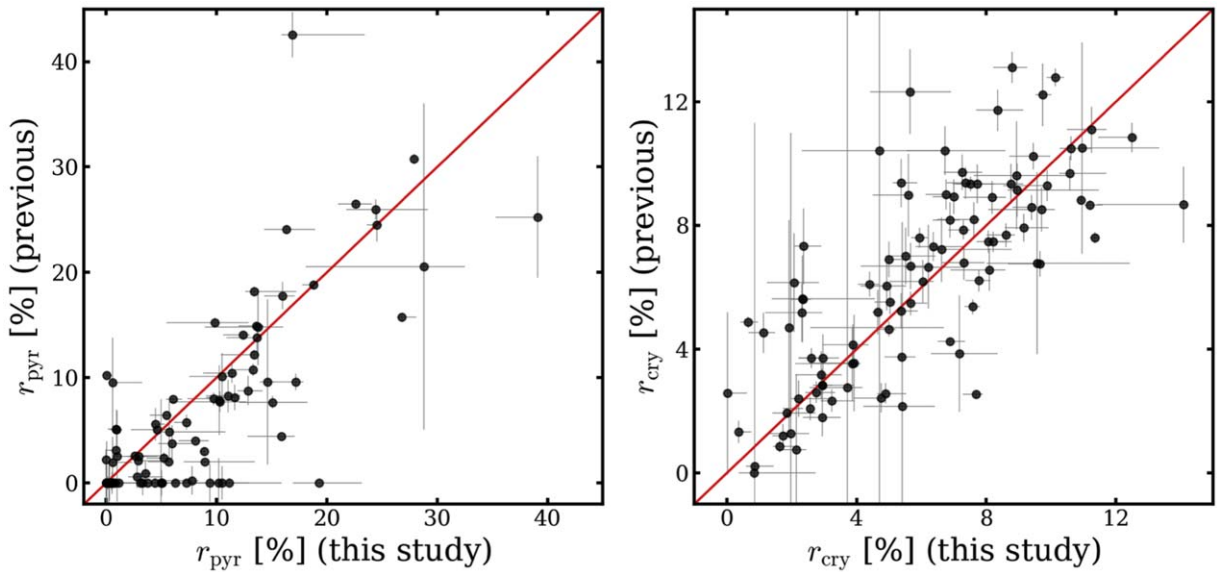


Figure 7. Correlation plots of the pyroxene mass fraction, r_{pyr} , and the crystallinity, r_{cry} , between the results of the previous studies and ours. Note that Tsuchikawa et al. (2021) defined the pyroxene mass fraction with the total mass of amorphous and crystalline silicate, while the present study defines r_{pyr} with the total mass of amorphous silicate. Therefore, we converted the pyroxene mass fraction obtained in Tsuchikawa et al. (2021) to the present definition in this figure.

small distortions of the feature profiles due to the radiative transfer effects were not considered in the previous study at all. Tsuchikawa et al. (2021) obtained the crystallinity by comparing the $10\ \mu\text{m}$ amorphous and the $23\ \mu\text{m}$ crystalline features. In principle, the radiative transfer affects the apparent optical depth ratio of two features with different wavelengths, as mentioned in Sections 1 and 3; however, the difference in the degree of the radiative transfer effects between the sample galaxies was not taken into account in the previous results of crystallinity. In contrast, our analysis takes the radiative transfer into account and therefore can reproduce the full-range IRS spectra.

In order to verify the validity of the results by Tsuchikawa et al. (2021), we compare both results in Figure 7. Note that the pyroxene mass fraction in the previous study is defined with the total mass of amorphous and crystalline silicate, while r_{pyr} in the present study is defined with the total mass of amorphous silicate. Therefore, the pyroxene mass fraction is recalculated with the mass column densities of amorphous olivine and pyroxene obtained in the previous study, according to the definition in the present study. Figure 7 shows that most of the objects are located around the diagonal lines. Thus, the approximations by Tsuchikawa et al. (2021) are reasonable to some extent as a method to systematically analyze the silicate absorption feature of heavily obscured AGNs. Nevertheless, Figure 7 shows significant scatters from the diagonal lines. The scatters indicate that the degree of the radiative transfer effects, which reflect the geometrical distribution of the dust density and temperature, is different between the individual objects. Hence, the present study is likely to derive the dust properties more reliably than the previous one.

5. Discussion

We discuss overall properties of silicate dust in heavily obscured AGNs below. Variations of the properties among heavily obscured AGNs are shown and possible causes of the variations are mentioned in the Appendix, where we cannot

obtain significant ($r > 0.7$; r is the Pearson's correlation coefficient) relationships with environmental parameters.

5.1. Amorphous Silicate

The pyroxene mass fraction was obtained reliably by the full-range spectral modeling of the mid-IR spectra considering the radiative transfer effects. The red dashed lines in Figure 6 correspond to the dust properties of the typical diffuse ISM in our Galaxy obtained in the sightline toward Sgr A* by Do-Duy et al. (2020). It is found that 90% of the sample galaxies show r_{pyr} lower than 17%, which is a value typical of the diffuse ISM in our Galaxy (Do-Duy et al. 2020). Thus, amorphous silicate dust in heavily obscured AGNs tends to have notably pyroxene-poor mineralogy compared to that in the diffuse ISM in our Galaxy.

It is known that amorphous pyroxene tends to be extremely poor in the circumstellar environments of evolved stars (e.g., Demyk et al. 2000; Do-Duy et al. 2020). The famous spectral profile of the silicate feature in the sightline toward the red supergiant η Cep star is reproduced well by amorphous olivine alone (Sargent et al. 2006). Ferrarotti & Gail (2001) theoretically predict the olivine-rich trend in the stellar ejecta of mass-loss stars with high mass-loss rates; olivine condensates earlier than pyroxene, and the radiation pressure on the olivine accelerates the wind material before pyroxene sufficiently condensates. On the other hand, amorphous pyroxene as well as amorphous olivine is needed to reproduce silicate features as seen in molecular clouds and the circumstellar space around YSOs (e.g., Demyk et al. 1999; van Breemen et al. 2011; Do-Duy et al. 2020). Based on such trends, it is believed that amorphous silicate evolves from olivine to pyroxene in the ISM (Demyk et al. 2001). The conversion of amorphous olivine to pyroxene occurs due to the selective sputtering of oxygen atoms, for example, by cosmic ray bombardments (e.g., Demyk et al. 2001; Carrez et al. 2002; Rietmeijer 2009). Therefore, silicate dust in heavily obscured AGNs on average is considered to be newly formed in the stellar ejecta and not processed much. On the basis of a merger-

induced evolutionary scenario, obscuring materials of heavily obscured AGNs are likely to have been newly supplied by the recent nuclear starburst activities.

In addition, we investigate two of the properties of amorphous silicate, namely the size distribution and the porosity. It is concluded that the porosity of silicate dust needs to be introduced because the DHS model ($f_{\text{max}} = 0.7$) is favored as a result of the full-range spectral modeling. For various astronomical objects in our Galaxy, such as the diffuse ISM, YSOs, evolved stars, and comets, the peak wavelength of the amorphous $18\ \mu\text{m}$ feature cannot be reproduced well by a homogeneous spherical dust model calculated by the simple Mie theory but the DHS model or other models with an internal inhomogeneity (e.g., Min et al. 2007). Hence, silicate dust in heavily obscured AGNs is probably of high porosity as well.

It is also found that the sample spectra of heavily obscured AGNs do not suggest micron-sized large silicate dust. Large-sized silicate is often observed in circumstellar disks on the basis of the peak shifts of the mid-IR silicate features (e.g., van Boekel et al. 2005; Juhász et al. 2010). Large-sized silicate dust is also introduced to reproduce the mid-IR spectra of optically classified type-1 AGNs or QSOs (e.g., Smith et al. 2010; Shi et al. 2014; Xie et al. 2017), while it is not likely to be needed for optically classified type-2 AGNs because the peak wavelengths of their silicate features tend not to shift (e.g., Hatziminaoglou et al. 2015). The difference in the grain size estimated from the mid-IR silicate features is likely to depend on regions where the features originate. Actually, most of the silicate features suggesting grain growth in optically classified type-1 AGNs, QSOs, and circumstellar disks are observed as emission, not absorption, which originates from dust located in inner hot regions. Hence, the silicate absorption features of optically classified type-2 AGNs and heavily obscured AGNs reflect properties of dust located in relatively outer cool regions, where grain growth is not likely activated because gas density is lower than that in inner hot regions. Accordingly, the small-sized and porous silicate that is suggested by the full-range modeling consistently supports the scenario that the pyroxene-poor silicate that obscures the AGNs is newly formed, originating from mass-loss stars in the recent starburst activity.

5.2. Crystalline Silicate

In our Galaxy, crystalline silicate is abundant only in the circumstellar space around evolved stars and YSOs, the crystallinities of which are 10%–15% and a few–40%, respectively (Henning 2010); the ISM silicate in our Galaxy is known to show almost no crystalline signature. For example, Do-Duy et al. (2020) and Min et al. (2007) obtained low mass abundances of crystalline silicate, $1.4\% \pm 0.2\%$ and $\sim 1\%$, respectively, in the line of sight toward Sgr A*. Therefore, the cosmic silicate is considered to be rich in the crystalline phase only immediately after the mass ejection by mass-loss stars, and then rapidly processed to the amorphous phase in the interstellar spaces due to cosmic ray bombardments (e.g., Demyk et al. 2001; Kemper et al. 2004; Branga et al. 2007). In the circumstellar space of YSOs such as protoplanetary disks, amorphous silicate is supplied from the interstellar space, and then crystallized due to thermal annealing in the hot environment close to the central star (e.g., Gail 2004).

We find that the crystallinity in heavily obscured AGNs is distributed widely from 0% to 14%. Based on the scenario that

silicate in heavily obscured AGNs is relatively fresh dust through the recent starburst activity, the crystallinity higher than 10% in the sample is expected to be attributed to the silicate originating from mass-loss stars. However, cosmic ray bombardments can completely amorphize the crystalline silicate on a short timescale of ~ 70 Myr in our Galaxy (Branga et al. 2007). Indeed, Kemper et al. (2011) simulated whether or not such high crystallinity can be achieved in starburst galaxies, considering the balance of production, destruction and amorphization of silicate. They concluded that the crystallinity higher than 10% observed in heavily obscured AGNs is difficult to reproduce via starburst activity alone. Thus, it is likely that the silicate dust in the heavily obscured AGNs is not only newly formed through the starburst activity but also crystallized later by other mechanisms, such as thermal annealing.

Amorphous silicate crystallizes at around 1000 K. On the other hand, in heavily obscured AGNs, because the mid-IR $23\ \mu\text{m}$ spectral bands due to crystalline silicate are detected only in the absorption, the crystalline silicate is likely to be located in outer cool regions compared to the vicinity of nucleus, as also pointed out by Spoon et al. (2006). A candidate mechanism of recrystallization in cooler regions is an in situ crystallization due to transient heating caused by shock waves (Harker & Desch 2002), which can be driven by outflows. Indeed, outflows are detected in many of the sample galaxies, and shock heating is predicted, for example, through mid-IR pure rotational molecular hydrogen lines (e.g., Hill & Zakamska 2014). The annealing time of the transient heating is expected to be so short that the chemical equilibrium cannot be achieved, and hence crystalline enstatite, the Mg end member of crystalline pyroxene, is unlikely to be formed (Gail 2004). Therefore, no detection of crystalline enstatite, which peaks at the wavelengths of, e.g., 18.5, 28, and $36\ \mu\text{m}$, in our sample spectra reasonably supports the in situ crystallization.

For another recrystallization mechanism of amorphous silicate in cooler regions in heavily obscured AGNs, we consider that amorphous silicate is crystallized in the high-temperature environments in the vicinity of the nucleus and then transported to a cooler outer region. Indeed, crystalline forsterite is detected in a quasar wind spectrum (Markwick-Kemper et al. 2007). However, Spoon et al. (2006) mentioned that the recrystallization mechanism is not plausible, because a large-scale transportation mechanism itself needs to be introduced. Nevertheless, as already mentioned above, recent observations have revealed that outflows are ubiquitously present in the nuclear regions of ULIRGs (e.g., Veilleux et al. 2020). Therefore, circumnuclear material may have experienced a large-scale transportation, and thus crystalline silicate could possibly have been transported. Given the high crystallinity in spite of the large-scale transportation, the timescale of amorphization must be longer than that of the outflow transportation to the outer cool region. For instance, the presence of a highly collimated molecular jet in the nuclear region of NGC 1377 is reported with ALMA (Aalto et al. 2012, 2016, 2020). The scale and age of the outflow are found to be 200 pc and 1.4 Myr, respectively (Aalto et al. 2012). On the other hand, the dust temperature at inner 3 pc is likely to be ~ 180 K, which should contribute to the mid-IR continuum emission. Comparing these outflow parameters with a typical amorphization timescale of 70 Myr due to cosmic ray

bombardments in our Galaxy (Bringa et al. 2007), the size of the mid-IR emitting layer is small enough to supply silicate dust with high crystallinity via transportation.

6. Conclusions

Various properties of silicate dust are imprinted on the profiles of the silicate absorption features observed in the mid-IR spectra of heavily obscured AGNs. We have selected 98 heavily obscured AGNs that show notably deep silicate absorption features in the mid-IR spectra observed by Spitzer/IRS. From the sample spectra, properties of the silicate dust in heavily obscured AGNs have been estimated systematically by the full-range 5–30 μm spectral modeling. The properties of silicate dust thus obtained are the pyroxene mass fraction r_{pyr} , the crystallinity r_{cry} , the size distribution, and the porosity. The results obtained in this study are summarized below.

1. Three dust species of amorphous olivine, amorphous pyroxene, and crystalline forsterite are needed to account for the differences in the silicate features. Their composition ratios widely vary among the sample galaxies. The median r_{pyr} is 5.1%, while several sources show significantly high values around 30%. The r_{cry} almost uniformly distributes in a range of 0%–14%.
2. Comparing the results of the mid-IR full-range spectral modelings between four dust models with different sizes and porosities, 97% of the sample galaxies prefer the porous silicate dust model without micron-sized large grains. The r_{pyr} and r_{cry} obtained by the full-range spectral modeling are overall consistent with the results obtained by the narrow-range 5.3–12 μm spectral modeling, but more reliable than the latter results for the individual galaxies.

Comparing the overall dust properties in heavily obscured AGNs with those in our Galaxy, we discuss the origin of the properties of silicate in heavily obscured AGNs, as summarized below.

1. The overall pyroxene-poor mineralogical composition, small dust size, and porosity of silicate dust in heavily obscured AGNs are similar to the circumstellar silicate ejected from mass-loss stars in our Galaxy. This trend suggests that silicate in heavily obscured AGNs is newly formed dust, which is presumably due to the recent circumnuclear starburst activity, considering the merger-induced evolutionary scenario.
2. The crystalline silicate in heavily obscured AGNs is likely to be located in outer regions cooler than the crystallization temperature, because the 23 μm crystalline band in heavily obscured AGNs is detected only in the absorption. In order to explain r_{cry} being higher than 10%, we propose two crystallization scenarios: one is the combination of thermal processing in the center and radial transportation of the crystalline silicate by outflows, and the other is the in situ transient heating of silicate by shocks originating from outflows.

This study is based on observations with the Spitzer Space Telescope, which is operated by the Jet Propulsion Laboratory, California Institute of Technology under a contract with NASA, using the Combined Atlas of Sources with Spitzer

IRS Spectra (CASSIS). CASSIS is a product of the IRS instrument team, supported by NASA and JPL. This study was supported by Grant-in-Aid for JSPS Fellows No. 21J14438.

Facility: Spitzer(IRS).

Software: DUSTY (Ivezic & Elitzur 1997), Emcee v3(Goodman & Weare 2010; Foreman-Mackey et al. 2013).

Appendix A

Variations in the Properties of Silicate Dust in Heavily Obscured AGNs

We find that there are significant variations in the pyroxene mass fraction, r_{pyr} , and the crystallinity, r_{cry} . The variations imply the processing of silicate dust in different environments among the individual heavily obscured AGNs. Therefore, we compare them with the statistical properties of the sample galaxies in order to better comprehend the nature of the properties of silicate dust.

A.1. Evolutionary Scenarios

Table 1 summarizes the total 8–1000 μm IR luminosity, L_{IR} , which generally reflects the total power of SF and AGN activities, for 97 out of all the 98 sample galaxies. L_{IR} in the sample galaxies ranges widely over three orders of magnitude from $1.5 \times 10^{10} L_{\odot}$ for NGC 1377 to $8.8 \times 10^{12} L_{\odot}$ for IRAS F00183-7111. Figure 8 shows the relations of the dust properties with L_{IR} , indicating a negative tendency between r_{pyr} and L_{IR} ($r = -0.46$ and $p = 1.9 \times 10^{-6}$, where r and p correspond to the Pearson’s correlation coefficient and the p -value, respectively), while r_{cry} does not show any tendency with L_{IR} ($r = -0.15$, $p = 0.14$). As shown in the left panel of Figure 8, the negative tendency is likely to be attributed to the low- L_{IR} galaxies with $\log_{10}(L_{\text{IR}}/L_{\odot}) < 11.2$. There are six pyroxene-rich sources, which show $r_{\text{pyr}} > 20\%$ in Figure 8; only one of them has relatively high L_{IR} , while all the other sources have low L_{IR} ($\log_{10}(L_{\text{IR}}/L_{\odot}) < 11.2$). Thus, silicate dust in the low- L_{IR} obscured AGNs is expected to be relatively old, according to the mineralogical evolutionary picture (see Section 5.1; Demyk et al. 2001). Relatively high- L_{IR} sources probably evolve through gas-rich mergers, whereas the low- L_{IR} sources are unlikely to experience such gas-rich mergers (Blecha et al. 2018; Kim et al. 2021). Taking into account that gas-rich mergers activate the circumnuclear star formations, low- L_{IR} obscured AGNs are likely to be deficient in newly formed dust, which could reasonably explain the low- L_{IR} obscured AGNs having relatively old silicate dust.

A.2. Evolutionary Stages

As the evolutionary stage advances, ionized gas outflows should be developed, resulting in less obscuration. Therefore, the optical depth of the silicate absorption feature can be regarded as an indicator of the evolutionary stage of heavily obscured AGNs. Indeed, Spoon et al. (2009) and Spoon & Holt (2009) found that the two galaxies, IRAS F00183-7111 and IRAS 12127-1412, which are thought to be in relatively advanced evolutionary stages because of the signatures of the ionized gas outflows, show mild silicate absorption compared to other heavily obscured AGNs in the mid-IR classification diagram of Spoon et al. (2007). Figure 9 shows the relation between the dust properties of the relatively high- L_{IR} sources with $\log_{10}(L_{\text{IR}}/L_{\odot}) > 11.2$, which do not show unusually high r_{pyr} in Figure 8, and the optical depth of the 10 μm silicate

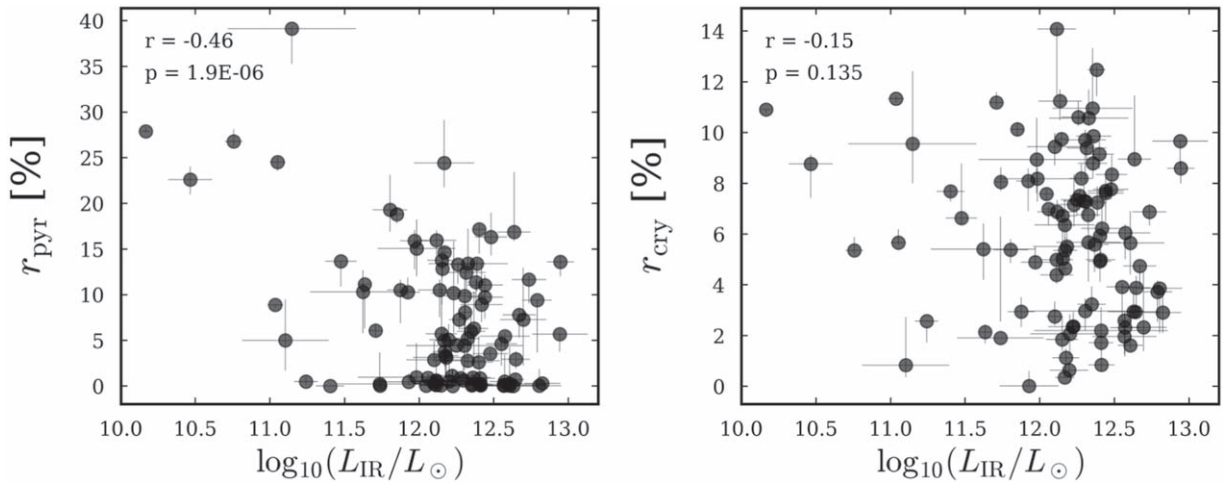


Figure 8. Properties of silicate dust as a function of the total infrared luminosity, L_{IR} , shown together with the Pearson’s correlation coefficient and the p -value in the top left corner.

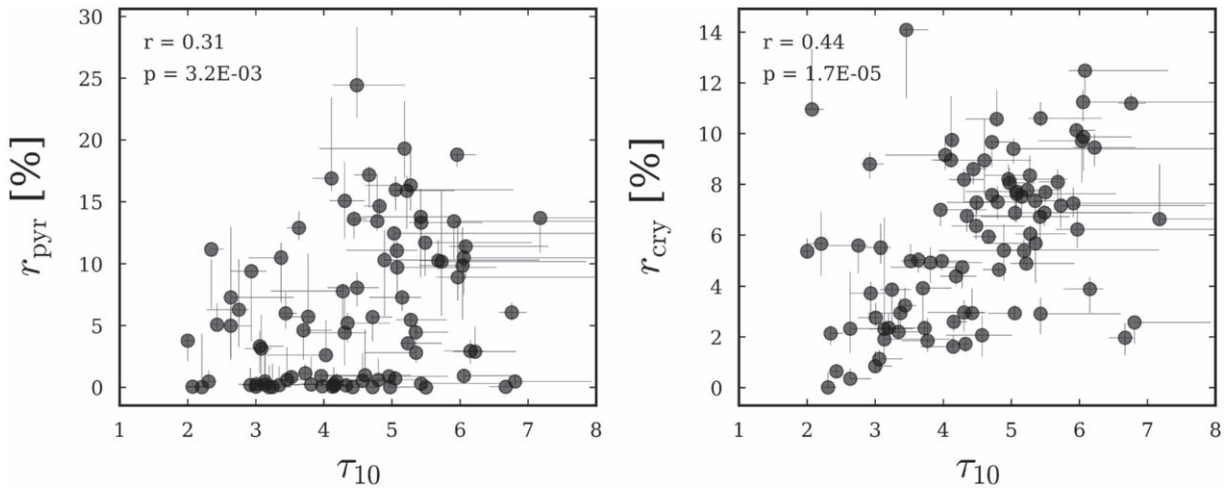


Figure 9. Relations of the properties of silicate with the optical depth of the $10\ \mu\text{m}$ silicate absorption feature, τ_{10} , shown only for high- L_{IR} sources with $\log_{10}(L_{\text{IR}}/L_{\odot}) > 11.2$. The Pearson’s correlation coefficient and the p -value are shown in the top left corner.

absorption feature, τ_{10} , as summarized in Table 5. Here, τ_{10} is calculated in the same way as performed for the sample selection in the previous and present studies, but using the best-fit model obtained in this study with the corrections for the PAH, line, and unobscured emission and ice absorption components. It is found that r_{pyr} and r_{cry} show positive tendencies ($r = 0.31$, $p = 0.0032$, and $r = 0.44$, $p = 1.7 \times 10^{-5}$, respectively). Thus, we consider a possible scenario where the amorphous pyroxene and crystalline silicate are less abundant in later evolutionary stages for the relatively high- L_{IR} sources, which are likely to have experienced the gas-rich merger and starburst activity.

The mineralogical evolutionary scenario predicts that pyroxene-rich silicate is relatively older (Demyk et al. 2001), as already mentioned in Section 5.1. Therefore, high- L_{IR} sources in later stages are possibly lacking in old amorphous silicate. This can be reasonably explained by a dynamical evolutionary picture that pyroxene-rich old silicate could be blown out by outflows with the evolutionary time and replaced by the newly formed pyroxene-poor silicate that originates from the recent starburst activity and has been supplied into the obscuring clouds.

The trend that the crystallinity decreases as τ_{10} decreases can be explained by considering the X-ray-induced amorphization (Ciaravella et al. 2016; Gavilan et al. 2016). In our Galaxy, Glauser et al. (2009) reported negative correlations of the X-ray luminosity and hardness with the crystallinity of the circumstellar silicate associated with class II YSOs. The amount of the material absorbing X-ray from the central engine decreases with the evolutionary time. In the case of heavily obscured AGNs, X-ray fluxes in the nuclear region can also increase with the SMBH growth. Accordingly, the X-ray photons can affect a larger fraction of the obscuring clouds in later evolutionary stage.

A.3. Orientation Effects

A spherically symmetric distribution is assumed for the density and temperature of the circumnuclear dust in the spectral modeling in this study, for simplicity. In reality, the existence of the outflows and the AGN unified scheme call for an axisymmetric but not spherically symmetric structure, as the crystallization scenarios proposed in Section 5.2 are associated with outflows. Hence, it is important to examine the

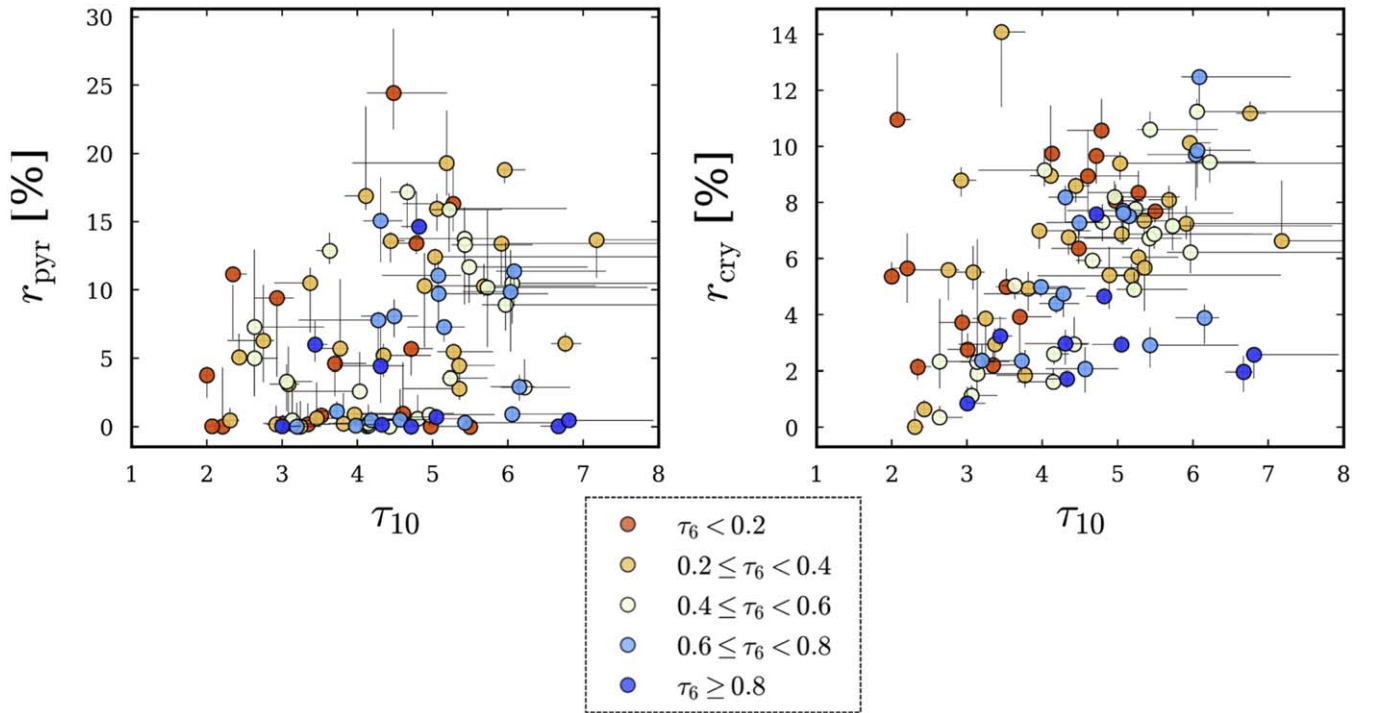


Figure 10. Same as Figure 9, but the data points are color-coded according to the optical depth of the $6\ \mu\text{m}$ H₂O ice absorption, τ_6 .

dependence on the orientation to confirm the validity of the scenarios.

In Figure 10, we color-code the data points in Figure 9 according to the optical depth of the $6\ \mu\text{m}$ H₂O ice absorption, τ_6 , as summarized in Table 5. The figure exhibits systematic differences in the distribution of the data points between galaxies with small τ_6 and those with large τ_6 . We perform a Kolmogorov–Smirnov test to verify the significance of the differences between the samples with $\tau_6 < 0.4$ and $\tau_6 > 0.6$. As a result, we find that the distribution of r_{cry} is different between the samples ($p = 0.023$), while that of r_{pyr} is not ($p = 0.18$). H₂O ice can exist only in regions colder than the sublimation temperature of 90 K (Tielens 2005). Such cold regions are likely to be located in the direction relatively perpendicular to the outflows, because the collisional heating by shocks should be less efficient in a direction closer to the edge-on view. The

X-ray heating is also inefficient in the edge-on direction, because of the large gas column density. Therefore, the trend of low r_{cry} for ice-rich sources suggests that crystalline silicate is richer in regions closer to the outflow directions, which can be consistently explained by the crystallization scenarios proposed in Section 5.2.

Appendix B Summary of all the Fitting Results

We perform the spectral modeling to determine the dust properties in heavily obscured AGNs. The pyroxene mass fraction, r_{pyr} , and the crystallinity, r_{cry} , thus obtained are summarized in Table 5, which also includes the optical depths of the $10\ \mu\text{m}$ silicate and the $6\ \mu\text{m}$ H₂O ice absorption features τ_{10} and τ_6 , respectively.

Table 5
Summary of the Dust Properties of the Sample




Name (1)	r_{pyr} (%) (2)	r_{cry} (%) (3)	τ_{10} (4)	τ_6 (5)
IRAS 00091–0738	7.28 ^{+0.40} _{-1.10}	7.52 ^{+0.22} _{-0.54}	5.15 ^{+0.28} _{-0.48}	0.69 ± 0.04
RAS F00183–7111	13.60 ^{+0.65} _{-1.58}	8.60 ^{+0.29} _{-0.59}	4.44 ^{+0.19} _{-0.10}	0.28 ± 0.01
IRAS 00188–0856	0.05 ^{+0.50} ₋₀	0.85 ^{+0.59} _{-0.26}	3.00 ^{+0.25} _{-0.00}	0.96 ± 0.02
IRAS 00397–1312	5.69 ^{+0.13} _{-1.95}	9.66 ^{+0.05} _{-0.98}	4.72 ^{+0.29} _{-0.02}	0.13 ± 0.01
IRAS 00406–3127	0.04 ^{+1.85} ₋₀	3.87 ^{+0.26} _{-1.76}	3.25 ^{+0.28} _{-0.17}	0.36 ± 0.02
AS 01166–0844SE	15.96 ^{+1.10} _{-1.66}	6.88 ^{+0.46} _{-0.36}	5.05 ^{+1.73} _{-0.00}	0.38 ± 0.04
IRAS 01199–2307	12.43 ^{+0.59} _{-1.84}	9.40 ^{+0.41} _{-0.59}	5.03 ^{+3.14} _{-0.00}	0.34 ± 0.04
IRAS 01298–0744	0.93 ^{+0.50} _{-0.58}	9.87 ^{+0.13} _{-1.34}	6.06 ^{+0.71} _{-0.00}	0.74 ± 0.02
IRAS 01355–1814	16.32 ^{+2.64} _{-2.03}	8.35 ^{+0.79} _{-0.66}	5.27 ^{+0.00} _{-0.67}	0.13 ± 0.07
IRAS F01478+1254	0.98 ^{+3.71} _{-0.34}	8.94 ^{+1.64} _{-1.32}	4.61 ^{+0.68} _{-0.71}	0.12 ± 0.09
IRAS 01569–2939	13.30 ^{+0.20} _{-2.12}	10.61 ^{+0.63} _{-0.34}	5.43 ^{+0.90} _{-0.18}	0.40 ± 0.03
IRAS 02455–2220	7.29 ^{+5.67} _{-5.07}	2.33 ^{+2.24} _{-0.94}	2.63 ^{+0.93} _{-0.01}	0.46 ± 0.17
IRAS 02530+0211	24.52 ^{+0.47} _{-0.92}	5.66 ^{+0.53} _{-0.07}	3.47 ^{+0.13} _{-0.07}	0.00 ± 0.00
IRAS 03158+4227	0.27 ^{+1.35} ₋₀	1.62 ^{+0.44} _{-0.19}	4.15 ^{+0.02} _{-0.48}	0.54 ± 0.04
NGC 1377	27.88 ^{+0.46} _{-0.10}	10.92 ^{+0.00} _{-0.12}	4.06 ^{+0.02} _{-0.02}	0.02 ± 0.01
IRAS 03538–6432	9.40 ^{+0.06} _{-5.72}	3.72 ^{+0.46} _{-1.17}	2.93 ^{+0.22} _{-0.31}	0.19 ± 0.03
IRAS 03582+6012	0.00 ^{+0.02} ₋₀	7.69 ^{+0.20} _{-0.41}	5.50 ^{+0.04} _{-0.03}	0.15 ± 0.00
IRAS 04074–2801	4.46 ^{+0.87} _{-0.30}	7.35 ^{+0.28} _{-0.58}	5.35 ^{+0.47} _{-0.02}	0.36 ± 0.02
IRAS 04313–1649	7.78 ^{+0.58} _{-2.46}	4.75 ^{+0.06} _{-0.84}	4.28 ^{+0.00} _{-1.06}	0.66 ± 0.10
IRAS 04384–4848	0.23 ^{+2.26} ₋₀	4.93 ^{+0.59} _{-0.80}	3.81 ^{+0.76} _{-0.19}	0.37 ± 0.05
ESO 203–IG001	18.80 ^{+0.20} _{-0.99}	10.13 ^{+0.27} _{-0.27}	5.96 ^{+0.28} _{-0.11}	0.34 ± 0.02
IRAS 05020–2941	11.38 ^{+0.32} _{-2.60}	12.49 ^{+0.13} _{-1.04}	6.08 ^{+1.22} _{-0.24}	0.62 ± 0.05
RAS F06076–2139	11.15 ^{+0.79} _{-4.81}	2.14 ^{+0.30} _{-0.45}	2.35 ^{+0.18} _{-0.00}	0.19 ± 0.04
IRAS 06206–6315	0.02 ^{+1.74} ₋₀	2.36 ^{+0.56} _{-0.29}	3.20 ^{+0.17} _{-0.14}	0.70 ± 0.04
IRAS 06301–7934	13.41 ^{+0.46} _{-3.03}	7.25 ^{+0.62} _{-0.56}	5.91 ^{+3.05} _{-0.00}	0.37 ± 0.07
IRAS 06361–6217	0.83 ^{+0.48} _{-0.68}	5.00 ^{+0.65} _{-0.11}	3.52 ^{+0.07} _{-0.14}	0.10 ± 0.02
1–0248	0.17 ^{+0.28} _{-0.12}	1.73 ^{+0.25} _{-0.32}	4.33 ^{+0.07} _{-0.26}	0.93 ± 0.03
01+2801	0.61 ^{+1.75} _{-0.20}	7.30 ^{+0.63} _{-0.68}	4.80 ^{+0.68} _{-0.48}	0.59 ± 0.07
0–6850	0.02 ^{+0.50} ₋₀	8.06 ^{+0.58} _{-0.36}	4.97 ^{+0.37} _{-0.03}	0.16 ± 0.01
72+3915	0.06 ^{+0.19} _{-0.03}	9.75 ^{+0.27} _{-0.22}	4.13 ^{+0.04} _{-0.02}	0.13 ± 0.01
39+0857	2.89 ^{+2.03} _{-0.28}	9.45 ^{+0.54} _{-0.74}	6.22 ^{+0.61} _{-0.32}	0.41 ± 0.05
8–3338	6.06 ^{+0.80} _{-0.65}	11.20 ^{+0.40} _{-0.16}	6.76 ^{+0.22} _{-0.18}	0.40 ± 0.01
91+4704	2.94 ^{+0.89} _{-1.04}	3.89 ^{+0.48} _{-0.95}	6.15 ^{+0.20} _{-0.38}	0.62 ± 0.08
73+0828	19.29 ^{+3.85} _{-2.38}	5.39 ^{+0.42} _{-0.52}	5.19 ^{+0.00} _{-1.25}	0.26 ± 0.16
37+4720	13.68 ^{+0.04} _{-2.80}	6.63 ^{+2.15} _{-0.23}	7.18 ^{+1.41} _{-0.00}	0.39 ± 0.03
78+1109	5.99 ^{+1.72} _{-1.25}	3.24 ^{+0.70} _{-0.35}	3.44 ^{+0.16} _{-0.08}	0.90 ± 0.04
5–1447	1.15 ^{+0.73} _{-0.86}	2.35 ^{+0.23} _{-0.40}	3.73 ^{+0.08} _{-0.50}	0.71 ± 0.06
28+3130	8.92 ^{+4.56} _{-1.90}	6.22 ^{+1.13} _{-0.74}	5.97 ^{+3.13} _{-0.31}	0.54 ± 0.20
38+3217	10.31 ^{+2.40} _{-4.53}	5.41 ^{+1.01} _{-1.21}	4.89 ^{+2.28} _{-0.00}	0.25 ± 0.10
5–0238	0.89 ^{+0.10} _{-0.77}	8.21 ^{+0.57} _{-0.13}	4.96 ^{+0.87} _{-0.00}	0.40 ± 0.02
0–2659	10.50 ^{+1.16} _{-2.97}	11.25 ^{+0.46} _{-0.75}	6.06 ^{+2.48} _{-0.00}	0.40 ± 0.05
80+1623	9.86 ^{+3.07} _{-4.40}	9.71 ^{+0.41} _{-1.64}	6.04 ^{+0.10} _{-0.64}	0.60 ± 0.12
3–1244	0.48 ^{+2.99} _{-0.12}	2.31 ^{+0.62} _{-1.13}	3.13 ^{+0.23} _{-0.22}	0.54 ± 0.06
06+1331	0.18 ^{+1.36} _{-0.04}	8.80 ^{+0.47} _{-0.59}	2.92 ^{+0.20} _{-0.13}	0.33 ± 0.03
24+1058	10.18 ^{+5.69} _{-4.37}	7.17 ^{+1.19} _{-0.87}	5.73 ^{+2.13} _{-0.00}	0.60 ± 0.19
82+3020	5.47 ^{+0.45} _{-1.48}	6.05 ^{+0.34} _{-1.03}	5.28 ^{+0.53} _{-0.22}	0.32 ± 0.03
32+1707	0.02 ^{+0.19} ₋₀	2.94 ^{+0.97} _{-0.17}	4.42 ^{+0.18} _{-0.14}	0.52 ± 0.03
7–1412	5.08 ^{+1.70} _{-0.40}	0.65 ^{+0.32} _{-0.24}	2.43 ^{+0.05} _{-0.07}	0.35 ± 0.01
4–0624	0.47 ^{+0.53} _{-0.33}	2.58 ^{+0.22} _{-0.84}	6.81 ^{+1.13} _{-0.00}	1.10 ± 0.04
GC 4418	8.90 ^{+0.08} _{-0.37}	11.34 ^{+0.10} _{-0.16}	4.53 ^{+0.03} _{-0.02}	0.62 ± 0.01
9–0725	3.13 ^{+2.73} _{-2.18}	5.52 ^{+0.93} _{-0.62}	3.08 ^{+0.15} _{-0.24}	0.38 ± 0.07
47+3721	24.43 ^{+4.72} _{-2.66}	6.36 ^{+0.99} _{-0.54}	4.48 ^{+0.71} _{-0.36}	0.00 ± 0.00
45+2354	0.02 ^{+4.30} ₋₀	5.66 ^{+1.25} _{-1.23}	2.21 ^{+0.08} _{-0.22}	0.17 ± 0.05
6–0922	0.05 ^{+0.36} _{-0.01}	1.97 ^{+0.57} _{-0.70}	6.67 ^{+0.12} _{-0.24}	1.20 ± 0.05
79+3401	22.62 ^{+1.43} _{-1.64}	8.77 ^{+0.38} _{-1.33}	6.39 ^{+1.40} _{-0.00}	0.43 ± 0.02
52+6402	4.62 ^{+1.05} _{-2.38}	3.92 ^{+0.11} _{-1.38}	3.70 ^{+0.42} _{-0.05}	0.14 ± 0.03
Mrk 273	12.88 ^{+1.31} _{-0.99}	5.04 ^{+0.14} _{-0.49}	3.63 ^{+0.08} _{-0.18}	0.53 ± 0.02

Table 5
(Continued)

Name (1)	r_{pyr} (%) (2)	r_{cry} (%) (3)	τ_{10} (4)	τ_6 (5)
70+0525	$0.31^{+0.52}_{-0.22}$	$2.91^{+0.63}_{-0.81}$	$5.43^{+1.18}_{-0.00}$	0.73 ± 0.05
94+5332	$0.24^{+0.64}_{-0.15}$	$2.76^{+0.58}_{-0.35}$	$3.01^{+0.06}_{-0.26}$	0.12 ± 0.02
11+1406	$0.47^{+0.91}_{-0.33}$	$0.02^{+0.60}_{-0}$	$2.31^{+0.12}_{-0.08}$	0.21 ± 0.02
54+3858	$5.00^{+4.50}_{-3.27}$	$0.84^{+1.89}_{-0.48}$	$3.71^{+0.32}_{-0.14}$	0.23 ± 0.04
25+2350	$3.33^{+1.20}_{-2.19}$	$1.13^{+0.36}_{-0.47}$	$3.06^{+0.34}_{-0.00}$	0.54 ± 0.04
50+3609	$0.02^{+0.15}_{-0.00}$	$7.58^{+0.22}_{-0.25}$	$4.72^{+0.07}_{-0.09}$	0.98 ± 0.02
Arp 220	$14.64^{+0.61}_{-0.71}$	$4.65^{+0.13}_{-0.17}$	$4.82^{+0.06}_{-0.23}$	0.88 ± 0.02
FESS J160655.82+541500.7	$28.80^{+3.70}_{-10.69}$	$4.70^{+3.89}_{-2.39}$	$1.61^{+0.51}_{-0.00}$	0.03 ± 0.04
RAS F16073+0209	$0.06^{+0.56}_{-0.00}$	$10.95^{+2.38}_{-0.00}$	$2.07^{+0.18}_{-0.09}$	0.00 ± 0.00
RAS 16090-0139	$0.12^{+0.26}_{-0.09}$	$2.60^{+0.26}_{-0.39}$	$4.15^{+0.20}_{-0.06}$	0.57 ± 0.02
RAS F16156+0146	$0.62^{+2.65}_{-0.06}$	$14.09^{+0.12}_{-2.69}$	$3.46^{+0.32}_{-0.06}$	0.32 ± 0.02
RAS F16242+2218	$0.22^{+3.46}_{-0}$	$1.91^{+4.78}_{-0}$	$3.14^{+1.03}_{-0.00}$	0.53 ± 0.21
RAS F16305+4823	$10.27^{+1.64}_{-0.72}$	$8.09^{+0.50}_{-1.19}$	$5.68^{+0.00}_{-0.27}$	0.20 ± 0.05
IRAS 16300+1558	$11.68^{+0.38}_{-2.62}$	$6.88^{+0.31}_{-0.54}$	$5.49^{+1.57}_{-0.00}$	0.51 ± 0.04
IRAS 16455+4553	$6.29^{+4.08}_{-3.03}$	$5.59^{+0.11}_{-1.09}$	$2.75^{+0.14}_{-0.47}$	0.21 ± 0.08
RAS 16468+5200W	$0.09^{+0.58}_{-0.03}$	$5.00^{+0.20}_{-0.37}$	$3.98^{+0.37}_{-0.10}$	0.75 ± 0.05
RAS 16468+5200E	$0.48^{+0.67}_{-0.35}$	$4.40^{+0.31}_{-0.36}$	$4.19^{+0.30}_{-0.23}$	0.67 ± 0.05
IRAS 17044+6720	$3.78^{+0.42}_{-1.68}$	$5.37^{+0.51}_{-0.25}$	$2.00^{+0.07}_{-0.07}$	0.06 ± 0.01
RAS F17028+3616	$39.11^{+0.31}_{-3.83}$	$9.57^{+2.86}_{-1.56}$	$2.59^{+0.07}_{-0.31}$	0.37 ± 0.09
IRAS 17068+4027	$2.61^{+2.85}_{-0.24}$	$9.16^{+0.77}_{-0.58}$	$4.03^{+0.00}_{-0.88}$	0.51 ± 0.03
RAS 17208-0014	$17.17^{+0.70}_{-2.67}$	$5.94^{+0.26}_{-0.25}$	$4.66^{+0.12}_{-0.22}$	0.52 ± 0.03
IRAS 17463+5806	$16.88^{+6.54}_{-1.02}$	$8.96^{+2.51}_{-0.30}$	$4.11^{+0.03}_{-0.28}$	0.38 ± 0.07
IRAS 17540+2935	$10.50^{+1.15}_{-3.61}$	$2.94^{+0.57}_{-0.60}$	$3.37^{+0.00}_{-0.48}$	0.23 ± 0.06
IRAS 18443+7433	$5.20^{+0.84}_{-1.56}$	$6.76^{+0.19}_{-0.62}$	$4.35^{+0.63}_{-0.00}$	0.33 ± 0.03
RAS 18531-4616	$2.80^{+2.30}_{-0.82}$	$5.67^{+0.50}_{-1.54}$	$5.35^{+0.00}_{-0.75}$	0.20 ± 0.07
IRAS 18588+3517	$15.90^{+1.19}_{-3.11}$	$4.90^{+0.63}_{-0.25}$	$5.22^{+0.71}_{-0.23}$	0.47 ± 0.05
RAS 20100-4156	$0.71^{+0.62}_{-0.58}$	$2.94^{+0.31}_{-0.28}$	$5.05^{+0.02}_{-0.39}$	1.24 ± 0.04
RAS 20109-3003	$15.07^{+3.17}_{-3.02}$	$8.19^{+0.42}_{-0.90}$	$4.31^{+0.29}_{-0.22}$	0.76 ± 0.29
IRAS 20286+1846	$0.53^{+2.25}_{-0.17}$	$2.07^{+0.77}_{-0.84}$	$4.57^{+0.44}_{-0.52}$	0.73 ± 0.13
RAS 20551-4250	$0.91^{+0.37}_{-0.77}$	$6.99^{+0.07}_{-0.64}$	$3.96^{+0.68}_{-0.00}$	0.26 ± 0.02
IRAS 21077+3358	$0.19^{+1.52}_{-0}$	$2.21^{+0.92}_{-0.22}$	$3.34^{+0.29}_{-0.11}$	0.11 ± 0.06
IRAS 21272+2514	$4.43^{+2.77}_{-2.70}$	$2.97^{+0.49}_{-0.76}$	$4.31^{+0.32}_{-0.54}$	0.88 ± 0.10
AS F21329-2346	$13.76^{+2.28}_{-4.82}$	$6.73^{+0.17}_{-1.18}$	$5.42^{+0.44}_{-0.87}$	0.51 ± 0.07
AS 22088-1831W	$11.05^{+1.09}_{-2.00}$	$7.72^{+0.54}_{-0.65}$	$5.07^{+0.31}_{-0.74}$	0.71 ± 0.07
AS 22088-1831E	$9.72^{+0.49}_{-2.36}$	$7.62^{+0.17}_{-1.12}$	$5.08^{+1.46}_{-0.00}$	0.72 ± 0.07
IRAS 22116+0437	$13.42^{+3.79}_{-0.80}$	$10.58^{+1.13}_{-0.33}$	$4.78^{+0.00}_{-0.45}$	0.04 ± 0.02
NGC 7479	$26.78^{+1.32}_{-0.47}$	$5.37^{+0.52}_{-0.16}$	$2.30^{+0.02}_{-0.10}$	0.11 ± 0.01
IRAS 23129+2548	$3.57^{+0.51}_{-0.54}$	$7.77^{+0.35}_{-0.40}$	$5.24^{+0.50}_{-0.11}$	0.53 ± 0.03
RAS F23234+0946	$5.72^{+5.09}_{-1.39}$	$1.85^{+0.89}_{-0.44}$	$3.77^{+0.10}_{-0.38}$	0.33 ± 0.07
RAS 23230-6926	$8.07^{+1.23}_{-1.52}$	$7.29^{+0.21}_{-0.46}$	$4.49^{+0.32}_{-0.34}$	0.72 ± 0.04
IRAS 23365+3604	$4.98^{+1.58}_{-2.57}$	$0.35^{+0.41}_{-0.02}$	$2.63^{+0.31}_{-0.00}$	0.42 ± 0.09

Note. Column 1: the name of the object. Column 2: the mass fraction of amorphous pyroxene to total amorphous silicate. Column 3: the mass fraction of crystalline silicate to total silicate dust. Columns 4 and 5: the optical depths of the 10 μm silicate and the 6 μm H₂O ice absorption features, respectively, which are used in Section 5.

ORCID iDs

T. Tsuchikawa  <https://orcid.org/0000-0002-0715-8244>
H. Kaneda  <https://orcid.org/0000-0001-6879-1556>
S. Oyabu  <https://orcid.org/0000-0003-4842-565X>
Y. Toba  <https://orcid.org/0000-0002-3531-7863>

References

- Aalto, S., Costagliola, F., Muller, S., et al. 2016, *A&A*, 590, A73
Aalto, S., Falstad, N., Muller, S., et al. 2020, *A&A*, 640, A104
Aalto, S., Muller, S., Sakamoto, K., et al. 2012, *A&A*, 546, A68
Blecha, L., Snyder, G. F., Satyapal, S., & Ellison, S. L. 2018, *MNRAS*, 478, 3056
Brandl, B. R., Bernard-Salas, J., Spoon, H. W. W., et al. 2006, *ApJ*, 653, 1129
Bringa, E. M., Kucheyev, S. O., Loeffler, M. J., et al. 2007, *ApJ*, 662, 372
Carrez, P., Demyk, K., Cordier, P., et al. 2002, *M&PS*, 37, 1599
Chiar, J. E., & Tielens, A. G. G. M. 2006, *ApJ*, 637, 774
Ciaravella, A., Cecchi-Pestellini, C., Chen, Y. J., et al. 2016, *ApJ*, 828, 29
Colangeli, L., Mennella, V., Palumbo, P., Rotundi, A., & Bussoletti, E. 1995, *A&AS*, 113, 561

- Demyk, K., Carrez, P., Leroux, H., et al. 2001, *A&A*, **368**, L38
- Demyk, K., Dartois, E., Wiesemeyer, H., Jones, A. P., & d'Hendecourt, L. 2000, *A&A*, **364**, 170
- Demyk, K., Jones, A. P., Dartois, E., Cox, P., & D'Hendecourt, L. 1999, *A&A*, **349**, 267
- Do-Duy, T., Wright, C. M., Fujiyoshi, T., et al. 2020, *MNRAS*, **493**, 4463
- Dorschner, J., Begemann, B., Henning, T., Jaeger, C., & Mutschke, H. 1995, *A&A*, **300**, 503
- Draine, B. T., & Hensley, B. S. 2021, *ApJ*, **909**, 94
- Draine, B. T., & Li, A. 2007, *ApJ*, **657**, 810
- Draine, B. T., Li, A., Hensley, B. S., et al. 2021, *ApJ*, **917**, 3
- Fabian, D., Henning, T., Jäger, C., et al. 2001, *A&A*, **378**, 228
- Ferrarotti, A. S., & Gail, H. P. 2001, *A&A*, **371**, 133
- Foreman-Mackey, D., Hogg, D. W., Lang, D., & Goodman, J. 2013, *PASP*, **125**, 306
- Gail, H. P. 2004, *A&A*, **413**, 571
- Gavilan, L., Jäger, C., Simonovici, A., et al. 2016, *A&A*, **587**, A144
- Glauser, A. M., Güdel, M., Watson, D. M., et al. 2009, *A&A*, **508**, 247
- Goodman, J., & Weare, J. 2010, *CAMCS*, **5**, 65
- Hagemann, H.-J., Gudat, W., & Kunz, C. 1975, *JOSA*, **65**, 742
- Hao, L., Weedman, D. W., Spoon, H. W. W., et al. 2007, *ApJL*, **655**, L77
- Harker, D. E., & Desch, S. J. 2002, *ApJL*, **565**, L109
- Hatziminaoglou, E., Hernán-Caballero, A., Feltre, A., & Piñol Ferrer, N. 2015, *ApJ*, **803**, 110
- Henning, T. 2010, *ARA&A*, **48**, 21
- Hill, M. J., & Zakamska, N. L. 2014, *MNRAS*, **439**, 2701
- Hopkins, P. F., Hernquist, L., Cox, T. J., et al. 2006, *ApJS*, **163**, 1
- Houck, J. R., Roellig, T. L., van Cleve, J., et al. 2004, *ApJS*, **154**, 18
- Hudgins, D. M., Sandford, S. A., Allamandola, L. J., & Tielens, A. G. G. M. 1993, *ApJS*, **86**, 713
- Ichikawa, K., Imanishi, M., Ueda, Y., et al. 2014, *ApJ*, **794**, 139
- Imanishi, M. 2009, *ApJ*, **694**, 751
- Imanishi, M., Dudley, C. C., & Maloney, P. R. 2006, *ApJ*, **637**, 114
- Imanishi, M., Maiolino, R., & Nakagawa, T. 2010, *ApJ*, **709**, 801
- Indebetouw, R., Mathis, J. S., Babler, B. L., et al. 2005, *ApJ*, **619**, 931
- Ivezic, Z., & Elitzur, M. 1997, *MNRAS*, **287**, 799
- Juhász, A., Bouwman, J., Henning, T., et al. 2010, *ApJ*, **721**, 431
- Kauffmann, G., Heckman, T. M., Simon White, D. M., et al. 2003a, *MNRAS*, **341**, 33
- Kauffmann, G., Heckman, T. M., Tremonti, C., et al. 2003b, *MNRAS*, **346**, 1055
- Kemper, F., de Koter, A., Waters, L. B. F. M., Bouwman, J., & Tielens, A. G. G. M. 2002, *A&A*, **384**, 585
- Kemper, F., Markwick, A. J., & Woods, P. M. 2011, *MNRAS*, **413**, 1192
- Kemper, F., Vriend, W. J., & Tielens, A. G. G. M. 2004, *ApJ*, **609**, 826
- Kennicutt, R., Jr., Armus, L., Bendo, G., et al. 2003, *PASP*, **115**, 928
- Kessler, M. F., Steinz, J. A., Anderegg, M. E., et al. 1996, *A&A*, **500**, 493
- Kim, E., Hwang, H. S., Jeong, W.-S., et al. 2021, *MNRAS*, **507**, 3113
- Lebouteiller, V., Barry, D. J., Spoon, H. W. W., et al. 2011, *ApJS*, **196**, 8
- Lutz, D. 1999, in *The Universe as Seen by ISO*, ed. P. Cox & M. Kessler, Vol. 427 (Paris, France: ESA Special Publication), 623
- Maaskant, K. M., Min, M., Waters, L. B. F. M., & Tielens, A. G. G. M. 2014, *A&A*, **563**, A78
- Mackie, C. J., Peeters, E., Bauschlicher, C. W., Jr., & Cami, J. 2015, *ApJ*, **799**, 131
- Markwick-Kemper, F., Gallagher, S. C., Hines, D. C., & Bouwman, J. 2007, *ApJL*, **668**, L107
- Marshall, J. A., Herter, T. L., Armus, L., et al. 2007, *ApJ*, **670**, 129
- Mathis, J. S., Rumpl, W., & Nordsieck, K. H. 1977, *ApJ*, **217**, 425
- Min, M., Hovenier, J. W., & de Koter, A. 2003, *A&A*, **404**, 35
- Min, M., Hovenier, J. W., & de Koter, A. 2005, *A&A*, **432**, 909
- Min, M., Hovenier, J. W., Dominik, C., de Koter, A., & Yurkin, M. A. 2006, *JQSRT*, **97**, 161
- Min, M., Waters, L. B. F. M., de Koter, A., et al. 2007, *A&A*, **462**, 667
- Molster, F. J., & Waters, L. B. F. M. 2003, in *The Mineralogy of Interstellar and Circumstellar Dust*, ed. T. K. Henning, Vol. 609 (Berlin: Springer), 121
- Murakami, H., Baba, H., Barthel, P., et al. 2007, *PASJ*, **59**, S369
- Pitman, K. M., Hofmeister, A. M., & Speck, A. K. 2013, *EP&S*, **65**, 129
- Rietmeijer, F. J. M. 2009, *ApJ*, **705**, 791
- Sanders, D. B., & Mirabel, I. F. 1996, *ARA&A*, **34**, 749
- Sargent, B., Forrest, W. J., D'Alessio, P., et al. 2006, *ApJ*, **645**, 395
- Schartmann, M., Meisenheimer, K., Camenzind, M., Wolf, S., & Henning, T. 2005, *A&A*, **437**, 861
- Shi, Y., Rieke, G. H., Ogle, P. M., Su, K. Y. L., & Balog, Z. 2014, *ApJS*, **214**, 23
- Siebenmorgen, R., Heymann, F., & Efstathiou, A. 2015, *A&A*, **583**, A120
- Siebenmorgen, R., & Krügel, E. 2007, *A&A*, **461**, 445
- SINGS Team 2020, Spitzer Infrared Nearby Galaxy Survey, IPAC, doi:10.26131/IRSA424
- Sirocky, M. M., Levenson, N. A., Elitzur, M., Spoon, H. W. W., & Armus, L. 2008, *ApJ*, **678**, 729
- Smith, H. A., Li, A., Li, M. P., et al. 2010, *ApJ*, **716**, 490
- Smith, J. D. T., Draine, B. T., Dale, D. A., et al. 2007, *ApJ*, **656**, 770
- Spoon, H. W. W., Armus, L., Marshall, J. A., et al. 2009, *ApJ*, **693**, 1223
- Spoon, H. W. W., & Holt, J. 2009, *ApJL*, **702**, L42
- Spoon, H. W. W., Marshall, J. A., Houck, J. R., et al. 2007, *ApJL*, **654**, L49
- Spoon, H. W. W., Tielens, A. G. G. M., Armus, L., et al. 2006, *ApJ*, **638**, 759
- Stierwalt, S., Armus, L., Charmandaris, V., et al. 2014, *ApJ*, **790**, 124
- Stierwalt, S., Armus, L., Surace, J. A., et al. 2013, *ApJS*, **206**, 1
- Tamanai, A., Mutschke, H., Blum, J., & Meeus, G. 2006, *ApJL*, **648**, L147
- Tielens, A. G. G. M. 2005, *The Physics and Chemistry of the Interstellar Medium* (Cambridge: Cambridge Univ. Press)
- Toba, Y., Bae, H.-J., Nagao, T., et al. 2017, *ApJ*, **850**, 140
- Tsuchikawa, T., Kaneda, H., Oyabu, S., et al. 2019, *A&A*, **626**, A130
- Tsuchikawa, T., Kaneda, H., Oyabu, S., et al. 2021, *A&A*, **651**, A117
- van Boekel, R., Min, M., Waters, L. B. F. M., et al. 2005, *A&A*, **437**, 189
- van Breemen, J. M., Min, M., Chiar, J. E., et al. 2011, *A&A*, **526**, A152
- Veilleux, S., Maiolino, R., Bolatto, A. D., & Aalto, S. 2020, *A&ARv*, **28**, 2
- Werner, M. W., Roellig, T. L., Low, F. J., et al. 2004, *ApJS*, **154**, 1
- Xie, Y., Li, A., & Hao, L. 2017, *ApJS*, **228**, 6
- Zeidler, S., Mutschke, H., & Posch, T. 2015, *ApJ*, **798**, 125